Monsoon-facilitated characteristics and transport of atmospheric mercury at a high-altitude background site in southwestern China

Hui Zhang[1], Xuewu Fu[1*], Che-Jen Lin[1,2], Lihai Shang[1], Yiping Zhang[3], Xinbin Feng[1*], Cynthia Lin[4]

[1] *State Key Laboratory of Environmental Geochemistry, Institute of Geochemistry, Chinese Academy of Sciences, Guiyang 550002, PR China.*

[2] *Center for Advances in Water and Air Quality, Lamar University, Beaumont, Texas 77710, United States.*

[3] *Xishuangbanna Tropical Botanical Garden, Chinese Academy of Sciences, Kunming 650223, China.*

[4]*The McKetta Department of Chemical Engineering, The University of Texas at Austin, Austin, Texas 78712, United States.*

Corresponding authors: Xinbin Feng (fengxinbin@vip.skleg.cn), Xuewu Fu (fuxuewu@mail.gyig.ac.cn)

Abstract

To better understand the influence of monsoonal climate and transport of atmospheric mercury (Hg) in southwestern China, measurements of total gaseous mercury (TGM, defined as the sum of gaseous elemental mercury, GEM, and gaseous oxidized mercury, GOM), particulate bound mercury (PBM) and GOM were carried out at Ailaoshan Station (ALS, 2450 m a.s.l.) in southwestern China from May 2011 to May 2012. The mean concentrations (±standard deviation) for TGM, GOM and PBM were 2.09±0.63 ng m^{-3}, 2.2±2.3 pg m^{-3} and 31.3±28.4 pg m^{-3}, respectively. TGM showed a monsoonal distribution pattern with relatively higher concentrations (2.22±0.58 ng m^{-3}, p=0.021) during the Indian summer monsoon (ISM, from May to September) and the East Asia summer monsoon (EASM, from May to September) periods than that (1.99±0.66 ng m^{-3}) in the non-ISM period. Similarly, GOM and PBM concentrations were higher in the ISM period than in the non-ISM period. This study suggests that the ISM and the EASM have a strong impact on long-range and transboundary transport of Hg between southwestern China and South and Southeast Asia. Several high TGM events were accompanied by the occurrence of northern wind during the ISM period, indicating anthropogenic Hg emissions from inland China could rapidly increase TGM levels at ALS due to strengthening of the EASM. Most of the TGM and PBM events occurred at ALS during the non-ISM period. Meanwhile, high CO concentrations were also observed at ALS, indicating that a strong south tributary of westerlies could have transported Hg from South and Southeast Asia to southwestern China during the non-ISM period. The biomass burning in Southeast Asia and anthropogenic Hg emissions from South Asia are thought to be the source of atmospheric Hg in remote areas of southwestern China during the non-ISM period.

1 Introduction

Mercury (Hg), because of its volatility and long residence time in atmosphere, can transport a long distance with air mass from anthropogenic Hg emission regions to remote areas (Schroeder and Munthe, 1998;Pirrone et al., 2010). The monsoonal climate has the potential to strongly affect the transport and distribution of atmospheric Hg in monsoon regions, such as East and South Asia. The onset of ISM in May causes air masses, originating from the Indian Ocean, to overpass South and Southeast Asia, and move northeastwardly to mainland China. Air pollutants such as SO_2 and CO also travel into Mainland China via air transport caused by the ISM (Xu et al., 2009;Bonasoni et al., 2010;Lin et al., 2013). In addition, the south tributary of westerlies, which passes over northern India and Myanmar into southwestern China, can also carry air pollutants to southwestern China and Tibetan plateau (Loewen et al., 2007;Xu et al., 2009;Yao et al., 2012). In East Asia, EASM is the dominant monsoon. During the monsoon period (from May to September), the warm and moist air masses from the Pacific Ocean sweep through the coastal area of China into inland China, and then move across southwestern China and the eastern Tibetan plateau. During the non-ISM period (from October to April), the dry and cold air masses from Siberia and Central Asia move through Mainland China into the Pacific Ocean via the westerlies (Hsu, 2005;Fan et al., 2013;Yu et al., 2015). The monsoonal wind changes play an important role in the transport of regional Hg emissions in Southeast and East Asia (Sheu et al., 2010a;Tseng et al., 2012;Lee et al., 2016).

An increasing number of studies have indicated that pollutant emissions and transport originate from developing countries in South and Southeast Asia (Wang et al., 2009;Lawrence and Lelieveld, 2010;Bonasoni et al., 2010;Wang et al., 2015), home to more than a billion people with strong energy demands, can impact other regions. These areas are regarded as important source regions of many air pollutants that pose significant health risk locally and regionally (Rajgopal, 2003;Lelieveld et al., 2001). Previous studies indicated that Hg emissions within South and Southeast Asia, including southwestern China, have significant impacts on the distribution and deposition of atmospheric Hg in South and East Asia (Pirrone et al., 2009;Mukherjee et al., 2009;Sheu et al., 2013;Fu et al., 2015;Zhang et al., 2012). These influences have raised concerns about high atmospheric Hg levels in India and Southwestern China, and increased Hg contents in the snow packs of Hindu Kush Himalayan-Tibetan glaciers (Loewen et al., 2005;Loewen et al., 2007;Kang et al., 2016). Previous studies reported that the open biomass burning in forests and agricultural waste burning in Southeast Asia are major sources for atmospheric Hg, aerosols and persistent organic pollutants in the region, which are subject to transboundary transport (Reid et al., 2013;Chang et al., 2013;Zhang et al., 2010;Sheu et al., 2013;Zhang et al., 2015;Wang et al., 2015). However, studies with respect to Hg emissions in South and Southeast Asia and the associated transboundary transport mediated by monsoonal weather are still lacking.

In this study, we conducted comprehensive measurements of TGM, GOM and PBM at Ailaoshan Station

(ALS), a remote site in Southwestern China. ALS is located in the subtropical mountainous region of Yunnan province and is close to South and Southeast Asia. The air flow to ALS is mainly controlled by the Indian monsoon climate with plenty of rainfall (85% of the total annual rainfall occurred during the ISM period) and also can be affected by EASM during the spring through early fall. In the winter, the weather is controlled by dry and cold monsoon circulation including westerlies and the cold Siberian current (Liu et al., 2003b;Yuhong and Yourong, 1993;Zhao et al., 2006). Therefore, ALS is as a unique location for studying the long-range and transboundary transport of Hg influenced by the ISM and the EAMS.

In this paper, we present the observations of TGM, GOM and PBM during the ISM and non-ISM periods at ALS, and discuss the transboundary transport characteristics using backward trajectory analysis. We also assess the potential contributing sources of Hg, and analyze the pathways of transboundary transport. This study is part of the Global Mercury Observation System (GMOS, http://www.gmos.eu/), which aims to establish a global mercury monitoring network for ambient concentrations and deposition of Hg though ground-based observational platforms, oceanographic and aircraft campaigns (Sprovieri et al., 2013)

2 Materials and methods

2.1 Measurement site descriptions

This study was conducted at Ailaoshan Mountain National Natural Reserve (24°32'N, 101°01'E) which lies in the Yunnan province of southern China, a protected forest section covering 5100 ha on the northern crest of a pristine evergreen broad-leaved forest on Mt. Ailao (23°35' –24°44' N, 100°54' –101°01' E). The forest altitude ranges from 2450 to 2650 m. above sea level (a.s.l.). The climate is influenced by both ISM and EASM during warm seasons with plenty of rainfall (Table 1). On the contrary, the dry and cold monsoon circulation from the south tributary of westerlies control the climate of Mt. Ailao in the winter (Table 1). Annual mean air temperature and rainfall in the study area are 11.3 °C and 1947 mm, respectively (You et al., 2012). Mt. Ailao is regarded as the largest tract (504 km^2) of natural evergreen broad-leaved forest and one of China's most important natural areas which has remained relatively undisturbed by human influences due to poor access (Liu et al., 2003a). Situated about 160 km to the south of Kunming, the capital of Yunnan province, ALS is relatively isolated from large anthropogenic Hg sources. The nearest populated center is Jingdong County (Population: 36500, 1200 a.s.l.), located 20 km to the south. Hg emissions in the Jingdong area is relatively low, ranging between 5-10 g km^{-2}, as displayed in Fig.1.

2.2 Sampling methods and analysis

2.2.1 Measurements of atmospheric TGM, GOM and PBM

From May 2011 to May 2012, TGM (GEM+GOM) in ambient air was measured every 5 minutes with an automated mercury vapor analyzer, Tekran Model 2537A (Tekran Inc., Toronto, Canada), which is widely used for monitoring atmospheric Hg. The automated instrument collects Hg on gold cartridges and then thermally

desorbs and detects the Hg by Cold Vapor Atomic Fluorescence Spectroscopy (CVAFS). The Tekran 2537A performs automatic calibration for TGM every 73 hours using an internal permeation source. To evaluate these automated calibrations, manual external injections using Tekran 2505 with known concentrations of Hg were performed every 4 months. PBM (≤0.2 μm) were collected using a 47 mm diameter Teflon filter (pore size 0.2 μm). To prevent the effect of Hg emission from ground and GOM sorption, the A Teflon sampling line with its inlet 5 m above the ground and heat preservation (50 °C) was employed at the sampling site. To mitigate the influence of low atmospheric pressure on the pump's strain, a low sampling rate of 0.75 L min^{-1} (at standard temperature and pressure)(Fu et al., 2008b;Swartzendruber et al., 2009;Zhang et al., 2015).

GOM and PBM was measured using a denuder-based system. The quartz denuders can collect GOM while air passes through the KCl-coated surfaces. However, GOM and PBM have extremely low concentrations and complex chemical reactivities in the atmosphere, and their chemical compounds are not well known. Several previous studies reported that different GOM compounds ($HgCl_2$, $HgBr_2$ and HgO) have different collection efficiencies for the KCl-coated denuder surface, as high relative humidity can passivate KCl-coated denuder and make GOM recoveries decrease (Huang et al., 2013a;Gustin et al., 2015;Huang and Gustin, 2015). In this study, the measurements of GOM and PBM were achieved by a manual method. The procedure of sampling and analysis of the manual method is analogous to the Tekran speciation system using identical denuders to the Tekran system with KCl coating (Gustin et al., 2015), differing only by manual operation. Details regarding the measurement system and the quality assurance routines are presented in earlier works (Xiao et al., 1997;Landis et al., 2002;Feng et al., 2000;Fu et al., 2012c;Zhang et al., 2015).

Four sampling campaigns were carried out for PBM and GOM measurements: August 17–24, 2011, December 3–17, 2011, April 12–19, 2012, and July 11–21, 2012. The selected periods represented the ISM period (May to September) and non-ISM period (October to April) observations. Before sampling, the denuders were pre-cleaned by pyrolysis to obtain the filed blanks, which was at 1.2 ± 0.7 pg (N=12) for denuders. The quartz fiber filter was heated at 900 ˚C for 30 minutes for pre-cleaning. A somewhat higher field blank (6.2 ± 2.7 pg, N=20) was observed and used to correct the PBM concentrations by subtracting the mean blank from the detected Hg. In this study, data QA procedure followed the GMOS Standard Operation Procedure and Data Quality Management (D'Amore et al., 2015).

2.2.2 Meteorological data and backward trajectory calculation

Meteorological parameters, including rainfall (RF), wind direction (WD), wind speed (WS), air temperature (AT) and relative humidity (RH), were provided by the local weather station from ALS. In order to identify the influence of long-range transport on the measured Hg at the study site, three-day backward trajectories were calculated using HYSPLIT and the Global Data Assimilation System (GDAS) meteorological data archives of

the Air Resource Laboratory, National Oceanic and Atmospheric Administration (NOAA). The meteorological data are of 1°×1° spatial resolutions at 6-hour intervals. All the backward trajectories ended at the sampling site at an arrival height of 500 m above the ground. The backward trajectories were calculated at 1-hour intervals, and cluster analysis of the trajectory endpoints was performed to determine the regional transport pathway. To distinguish the larger sources from moderate sources, a weighing algorithm based on measured concentrations (concentration weighted trajectory (CWT)) was applied in this study. In this procedure, each grid cell received a source strength obtained by averaging sample concentrations that have associated trajectories that crossed that grid cell as follows:

$$C_{ij} = \frac{1}{\sum_{l=1}^{M} \tau_{ijl}} \sum_{l=1}^{M} C_l \tau_{ijl}$$

C_{ij} is the average weighted concentration in the grid cell (i,j). C_l is the measured Hg concentration, τ_{ijl} is the number of trajectory endpoints in the grid cell (i,j) associated with the C_l sample, and M is the number of samples that have trajectory endpoints in grid cell (i,j). A point filter is applied as the final step of CWT to eliminate grid cells with few endpoints. Weighted concentration fields show concentration gradients across potential sources. This method helps determine the relative significance of potential sources (Hsu et al., 2003;Cheng et al., 2013).

3 Results and discussion

3.1. General distribution characteristics of TGM, GOM and PBM

The highly time-resolved long-term data set of TGM concentrations in ambient air at ALS is displayed in Fig. 2, and the mean TGM concentration over the sampling period was 2.09±0.63 ng m^{-3} with a higher level (2.22 ng m^{-3})during the ISM period than that during the non-ISM period (1.99 ng m^{-3}) (Table 1). The TGM mean concentration at ALS was slightly higher than that of the global background (1.5-1.7 ng m^{-3} in the Northern Hemisphere and 1.1-1.3 ng m^{-3} in the Southern Hemisphere (Lindberg et al., 2007;Slemr et al., 2015;Venter et al., 2015), and higher than those (1.58 to1.93 ng m^{-3}) observed in some remote areas in northern America and Europe (Kim et al., 2005;Sprovieri et al., 2010). Compared to the background concentrations observed at the Shangri-La Baseline Observatory in Yunnan province (2.55±0.73 ng m^{-3}, (Zhang et al., 2015), at Mt. Leigong in Guizhou province (2.80 ± 1.51 ng m^{-3}, (Fu et al., 2010b) and at Mt. Gongga in Sichuan province (3.98±1.62 ng m^{-3}, (Fu et al., 2008a), the mean TGM level at ALS was lower. However, the mean TGM level at ALS was higher than those observed at Mt. Changbai (1.60 ± 0.51 ng m^{-3}) in Northeast China and at Mt. Waliguan (WLG) Baseline Observatory (1.98 ± 0.98 ng m^{-3}) in the Tibetan plateau (Fu et al., 2012a;Fu et al., 2012b). Interestingly, most peaks of high TGM concentrations at ALS frequently appeared during the ISM period (Fig. 2). This differed from the previous results at Mt. Gongga and Mt. Leigong of southwestern China but was similar to the results at Shangri-La. There were also several peaks that appeared during the non-ISM period, which could have been caused by different sources than those during the ISM period. The sampling site is located adjacent to South Asia and Southeast Asia, and Hg emissions from biomass burning in South Asia and

Southeast Asia would inevitably contribute to the elevated TGM concentrations at ALS during the non-ISM period (Wang et al., 2015). Southwestern China is one of the largest Hg emission areas in China, and coal combustion and non-ferrous metal (especially zinc) smelting activities are the two main Hg sources. It was reported that total Hg emission from Guizhou, Sichuan and Yunan provinces reached about 128 tons in 2003 (Wu et al., 2006), and the large amount of Hg emissions contributed to the elevation of TGM concentrations in this area. Since Guizhou, Sichuan and Yunan provinces are located in the upper wind direction of the sampling site to EASM, Hg emission from these areas can be transported to ALS and result in the elevation of TGM concentrations.

Fig. 3 displays the distribution frequency of TGM above and under the average (2.09 ng m^{-3}) based on wind direction including Northeast (NE), Southeast (SE), Southwest (SW) during the ISM and non-ISM period. It is clear that SW was the predominating wind direction, and there was no Northwest (NW) during the entire study period. The SW frequency was highest when high and low TGM levels occurred during the ISM period or non-ISM period, and the SW frequency showing low TGM was higher than that of high TGM. This could be the reason why the average TGM level from SW was not high. The air flows originating from South Asia and Southeast Asia could contribute to high TGM concentrations at ALS. Contrarily, NE and SE frequency had a relatively lower trend than SW, but high TGM frequency from NE and SE were both high during the ISM period. This should be the result from the strengthening of EASM during the ISM period. However, during the non-ISM period, the cold and dry air flow from the south tributary of westerlies could have swept over South Asia and Southeast Asia and moved to ALS with high wind speed (Fig. 4). This dry air flow could have also taken the air masses of high Hg levels emitted from biomass burning in South Asia and Southeast Asia to ALS and caused a rapid increase of TGM level at ALS. In addition, cold air flows could also transport Hg emitted from inland China to ALS due to the strengthening of the cold Siberian current during the non-ISM period. Therefore, there were some high TGM events in December and March at ALS (Fig. 4).

For GOM and PBM, which on average accounted for <2% of the TGM, there were also seasonal trends. Both species had the highest levels in autumn while GOM was lowest in the winter and PBM was lowest in the spring. The lowest GOM level was observed in the summer, which increased consistently to reach the highest value (3.4±3 pg m^{-3}) in autumn. Similarly, PBM displayed the same distribution in seasonal variation, with the highest PBM level in autumn (46.3±28.8 pg m^{-3}). Meanwhile, the AT, RF and RH were also higher during the ISM period than those during the non-ISM period. However, unlike TGM, the GOM and PBM were closely linked with atmospheric Hg chemistry, meteorological patterns, and numerous other factors. Thus, there are several likely factors that contribute to these trends, including a greater number of sources during the ISM period, and changing ecological or meteorological conditions. Previous studies in the Mt. Gongga and Mt. Leigong area suggested that enhanced coal and biomass burning played a significant role in elevated TGM concentrations during cold seasons (Fu et al., 2008a;Fu et al., 2010a). Enhanced coal and biomass burning

during cold seasons is generally driven by the need for residential heating in China. However, in the southern Yunnan province, the air temperature is high during the non-ISM period. Thus, the domestic use of coal is not dominant for residential heating, but rather the agricultural activity in the region including the crop harvesting and the burning of straw. This was probably one of most important reasons for the highly elevated GOM and PBM level at ALS in autumn.

3.2 Seasonal variation of TGM, GOM and PBM influenced by monsoonal climate

Table 1 shows seasonal statistics of daily averages for Hg species and select meteorological parameters which were determined on a seasonal basis and for the year-long dataset. TGM during the ISM period was statistically higher than during the non-ISM period (Table S1). Meanwhile, AT, RF and RH had a distribution with the highest level during the ISM period, and SW frequency had decline with increase of SE and NE frequency during the ISM period. This suggests the EASM could also influence the climate at ALS during the ISM period, which was consistent with TGM concentration that the site is impacted by regional sources including biomass burning and monsoonal long-range transboundary transport.

To assess the monsoonal variation of TGM concentrations, the distribution of monthly mean TGM concentrations at ALS is shown in Fig. 4. The TGM concentrations during the ISM period were higher than those during the non-ISM period. The highest monthly concentration was observed in May with a mean value of 2.46 ng m^{-3}, and the lowest monthly mean concentration of 1.45 ng m^{-3} was observed in November. Although there were relatively higher TGM levels in December and January during the non-ISM period, this pattern was generally different from the most common pattern in the Northern Hemispheric which has a summer minimum and winter maximum TGM distribution pattern as observed in many previous studies (Kellerhals et al., 2003;Kock et al., 2005;Fu et al., 2010a). There were several possible reasons for this monsoonal distribution pattern of TGM concentrations on ALS.

Firstly, the increase of TGM concentrations during the ISM period could be due to the interaction of the EASM and the ISM, promoting the air masses with high TGM from the areas of anthropogenic Hg emissions to ALS. Generally, ALS is located on the low latitude highlands of Yunnan in southwestern China which is subject to the interactions between the EASM and the ISM, although most of time, the air flow of Yunnan is mainly controlled by the ISM during the ISM period. However the strengthening of the EASM or the weakening of the ISM can also spur the EASM to control this area and bring precipitation during the ISM period (Fan et al., 2013). Therefore, the TGM level should be sensitive to the strengthening/weakening of the two monsoons. Once the air flow from high Hg source regions (Sichuan, Guizhou and Chongqing) is transported to ALS with the strengthening of the EASM, TGM levels at ALS can increase rapidly. However, anthropogenic Hg emissions from inland China could increase the TGM background level with the raid of westerlies and cold Siberian current during the non-ISM period. Previous studies discussed the seasonal

change of TGM at the background sites of southwestern China and found that increased domestic coal consumption and an increase in household heating was the main cause of elevated TGM concentrations observed in winter (Fu et al., 2008a;Fu et al., 2010a). Additionally, the biomass burning in Southeast Asia could also be an important reason for high TGM level at ALS during the non-ISM period. Intense biomass burning originating from Southeast Asia typically occurred in late winter and spring (Huang et al., 2013b). This could be the cause of the high TGM at ALS along with the long-range transboundary transport in the spring (Wang et al., 2015).

Monsoonal distribution patterns and mean TGM, GOM and PBM concentrations based on the four sampling campaigns in ALS are shown in Fig. 5. Mean concentration of the three Hg species showed a monsoonal variation with higher levels during the ISM period than during the non-ISM period. This suggests that regional anthropogenic emissions are important Hg sources in southwestern China. During the ISM period, not only was air flow originating from the Indian Ocean dominating, but air flow that occasionally originated from the Pacific Ocean also intruded the study site, which passed through central and southwestern China, one of the most Hg-polluted regions. Moreover, the TGM, GOM and PBM levels from the north were higher than those from the south to ALS (Fig. S1). Thus, the air masses likely captured large amounts of Hg during transport and caused elevated atmospheric TGM concentrations at ALS during the ISM period.

Fig. 6 shows pollution roses of TGM, GOM and PBM at ALS during the ISM period and during the non-ISM period respectively. The wind direction at the study site was dominantly SW. This reflects that the predominant monsoon influencing the ALS site is the ISM and westerlies. During the ISM period, most of the TGM, GOM and PBM events were from SW, slightly fewer were from NE, and both SW and NE exhibited higher TGM, GOM and PBM events. This indicates SW and NE were the two primary directions of high Hg sources during the ISM period. However, during the non-ISM period, almost all TGM, GOM and PBM events were from SW. This indicates that strong westerlies were the primary winds during the non-ISM period. These westerlies could take the GEM and PBM from South Asia and Southeast Asia into southwestern China. Thus, the dependence of atmospheric Hg on wind was likely attributed to an interplay of regional sources and the long-range transboundary transport of the GEM and PBM.

Indeed, GOM concentrations were extremely low at ALS. Marine air masses during the ISM period likely diluted the atmospheric TGM in the study area. The high RF and low WS can promote the wet deposition of GOM and PBM. Therefore, in the summer, RH was very high, but the GOM and PBM were very low at ALS. A new study reported that high RH could reduce the collection of GOM by the KCl-coated denuder (Huang, Gustin et al. 2015). This could be another reason why the GOM was low in summer. Additionally, low GOM and PBM could be also related to rapid deposition of Hg due to the high altitude montane environment and luxuriant virgin forest cover of Mt. Ailao. A previous study already found that the increasing occurrence and

extension of fog and cloud droplet interception can enhance the uptake of Hg by foliage (Zhang et al., 2013). We will study the possible reasons why the GOM level is exceedingly low in ALS via continuous long-term monitoring for GOM in the future.

3.3 Transboundary transport of Hg facilitated by monsoons

The backward trajectories arriving at ALS over the study period were grouped into five clusters, which are shown in Fig. 7. Most of these backward trajectories consisted of air masses that originated from the South Asia and Southeast Asia, passing over India, Bengal Bay, the Indo-China peninsula and the southern Yunnan province of China. Just 4.7% of air masses originated from inland China and then passed over Sichuan, Guizhou, Yunnan provinces and the city of Chongqing, China. For the five types of air masses, air masses in cluster 1 displayed very low TGM concentrations (1.86 ng m^{-3}) for all the air masses, although their frequencies were the highest (38.55%). Similarly, the mean TGM concentration in cluster 3 was 1.92 ng m^{-3}, which was also considerably low and had second highest frequency (23.03%). This suggest that Hg emitted in South Asia could not have largely contributed to the high TGM levels at ALS. Air masses in cluster 4 showed a high TGM concentration of 2.42 ng m^{-3}, which originated over the South China Sea and passed over northern Vietnam and Laos and the southern Yunnan and Guangxi provinces of China, which are generally areas of less anthropogenic emissions other than biomass burning during the non-ISM period. However, the air masses in cluster 5 were also polluted with Hg, with a mean concentration of 2.20 ng m^{-3}, which is higher than those of clusters 1, 3 and 4. Air flows likely originated in Bengal Bay and passed over Myanmar since most anthropogenic emissions in Myanmar are centralized in southern Myanmar, and intense biomass burning in the area during the non-ISM period perhaps contributed to a slightly high TGM level of these air masses. Cluster 2 displayed the highest TGM concentrations (2.65 ng m^{-3}). Air masses in cluster 2 passed over the inland China region, which is the most densely populated and heavily Hg-polluted area in China due to industrial and domestic coal combustion, smelting industries, cement production, biomass burning, etc. Sichuan, Guizhou, Chongqing and the northwestern Yunnan provinces, respectively, were contributing Hg source provinces in China. Although only 4.70% of air masses were from the southwestern China region, the TGM concentrations of these air masses were the highest, which could be an important reason for elevated TGM levels at ALS.

The Tibetian plateau and Yunnan-Guizhou plateau are located in north of ALS, which is a monitoring site at high elevation. To the south of ALS, the geography consists of a montane area plain of low elevation. Thus, the air masses at ALS were from different directions and of different heights, which may have affected the TGM level in the air masses as they passed over different anthropogenic emission regions. Fig. S2 compares the three-dimensional height of all the wind clusters arriving at ALS. The height of cluster 1 from India was the highest. Such transport pattern tends to more effectively dilute Hg emissions from low altitude surface to ALS. Thus, in non-ISM period, the south tributary of westerlies passed over India does not lead to elevated TGM concentrations at ALS. Additionally, due to the high TGM concentration in the air in southwestern

China, the TGM level of any air masses coming from the northeast of ALS should be increased at ALS regardless of height. Contrarily, cluster 3 had a high height but low level TGM because its air masses originated and passed over the area of low anthropogenic emission region.

3.4 Impacts of Hg emission from industrial sources and biomass burning

Fig. 8 shows the seasonal trend analysis using the average of the daily TGM values, RF distribution, WS and WD during the study period along with IMI (Indian monsoon index) at ALS. In general, May to September represent the normal ISM period. The IMI, however, also illustrates the onset in of the ISM in May and its retreat at the end of September. During the ISM period, the mean TGM is 2.22 ng m^{-3}, which is slightly higher than 1.99 ng m^{-3} during the non-ISM period, and most of the RF events appeared during the ISM period. More crucially, some high-frequency NE and east wind events occurred during the ISM period. Once the WD shifted from SW to NE, the TGM level rapidly increased in addition to relatively lower RF and WS. This indicates that the strengthening of EASM can move the air masses with high TGM levels from inland China to ALS, but when the NE air flow climbed over the Yunnan-Guizhou plateau, the speed of air mass movement decreased and carried less RF. However, during the non-ISM period, the high TGM events did not accompany the appearance of NE. The WD was primarily SW other than a few SE at the end of March, and the WS was higher than the level during the ISM period. This indicates that the south tributary of westerlies could control the climate and carry air masses from South Asia and Southeast Asia. High TGM events were also evident with SW and SE during the non-ISM period, which could be due to Hg emission from biomass burning in South Asia and Southeast Asia.

Therefore, five special high TGM events were accompanied by an exceeding variation of WD and WS to analyze the reasons of high TGM appearance. As Fig. 8 shows, five extreme peaks of high TGM were displayed from June 23-29 and July 10-18, 2011, September 28 to October 9 and December 23-31, 2011, and March 23-29, 2012, respectively. On June 23, the air masses from India began to increase TGM concentrations, and with the strengthening of the EASM, the TGM level increased gradually and peaked with low RF and WS on June 26. The air masses that had just swept Chongqing, Sichuan, Guizhou and eastern Yunnan provinces, including Kunming city, where there is high Hg emission because of industrial activities (Fig. 1). Thus the air flow from these areas could suddenly increase the TGM level at ALS due to the long-range transport. Once the air flow from EASM faded away, the ISM would control the ALS area again, the air flow would shift to southwest, and the TGM level would return to average levels (Fig. 9a). The same variation appeared from July 10-18 during the ISM period. TGM levels increased on July 10 and were highest (3.65 ng m^{-3}) from July 14-16 with the strengthening of EASM. When WD shifted to SW, TGM was back to its base level (Fig. 9b). In fact, during the ISM period, this sort of peak appeared many times (Fig. 2), the reason for these peaks being similar to the two peaks in June and July.

However, on September 28, due to the fadeaway of ISM and the strengthening and incursion of air flow from EASM as well as the cold Siberian current, a high TGM event was initiated as the air flow shifted from SW to NE (Fig. 10). When the air flow swept Chongqing, Sichuan, Guizhou and eastern Yunnan province again from September 30 to October 5, the TGM level increased to its highest level (3.18 ng m^{-3}), then gradually decreased with the shift in air flow that swept northern Vietnam and Laos. These high TGM events happened during the transitional period from the ISM period to the non-ISM period, which indicates that the high Hg emission from inland China had severely influenced the TGM level at ALS. As previously discussed, the strengthening of the EASM or the weakening of ISM caused the air flow with high TGM originating from inland China to be transported to ALS, which contributed to extremely high TGM concentrations.

During the non-ISM period, with the fading of the ISM and EASM, the south tributary of westerlies grew stronger as the dry and cold air flow swept over South and Southeast Asia and arrived in southwestern China to control the climate. Hence, industrial sources likely contributed to the high level TGM concentrations in this study site. In Fig. 11, when air masses entered from important Southeast Asia industrial regions (e.g. Hanoi, Haiphong et al.), the TGM level was highest (3.13 ng m^{-3}) while TGM concentrations decreased 11% with the entrance of the strong wind from the Bay of Bengal. In addition, fire events were also observed along the backward trajectories. Moreover, the high correlation (R^2=0.89) between TGM and CO was identified in Fig. 12. However, the TGM/CO ratio was 0.01124 ng g^{-1} ppb^{-1} (1.80 E-6 mol mol^{-1}), which is more than 10 times higher than the reported world average biomass burning ratio but was close to ratios observed in Taiwan in October (1.28 E-6, verified from anthropogenic plumes) Sheu et al. (2010b);(Friedli et al., 2009). Therefore, in this event, the major contributor should be the industrial sources from Southeast Asia. Fig. 13 shows that biomass burning is an important source for TGM. On March 23, the high TGM concentrations began to arise because of the fire events that occurred in northeastern India and north Myanmar. TGM levels were highest (4.53 ng m^{-3}) when the air flow shifted and swept inland China. When the air flow shifted from east to southwest and swept south Myanmar from March 25-28, a period of were high-frequency fire events, the TGM concentrations maintained a high level (3.11 ng m^{-3}). However, when the air flow shifted to northern Myanmar, the TGM level returned to low levels (2.01 ng m^{-3}), indicating that biomass burning originating from Southeast Asia could also rapidly input and increase the TGM levels in southwestern China during the non-ISM period. Different from Fig. 12, the TGM/CO ratio decreased by half in Fig. 14 and was comparable with reported biomass burning ratios (3.00 E-7) in Canada and the USA (Sigler et al., 2003). Moreover, the close correlations between TFRP (total fire radiative power), which provides information on the measured radiant heat output of detected fires, and CO (R^2=0.98) and TGM (R^2=0.45) verify the above hypothesis (Wooster et al., 2005).

3.5 Potential source regions of atmospheric Hg

Fig. 15a shows the possible source regions and pathways of atmospheric TGM at ALS during the ISM period

identified by the CWT analysis. Sichuan, Guizhou, Chongqing, Yunnan and Guangxi provinces in southwestern China as well as in Southeast Asia as well as northern Laos, Cambodia, Thailand and Vietnam were likely source regions of high atmospheric TGM at ALS during the ISM period. Southwestern China, including Sichuan, Chongqing, Guizhou, and Yunnan provinces, is an important anthropogenic source region of China (Wang et al., 2006;Feng and Qiu, 2008;Wu et al., 2006;Jiang et al., 2006). In fact, several capital cities including Kunming, Guiyang and Chongqing are located about 200 to 800 km north of ALS. These capital cities may be the source of much of the Hg emissions during atmospheric transport. The identified source areas correspond very well with the anthropogenic Hg emission inventories in East and South Asia. The potential area identified in Southeast Asia is also classified as a high anthropogenic Hg emission region by Hg emission inventories (Pacyna et al., 2010;Pirrone et al., 2010;Li et al., 2009), and the biomass burning in Southeast Asia could cause high Hg emissions. During the non-ISM period, as displayed in Fig. 15b, Northern India is an important urbanized and industrialized area that may produce high anthropogenic Hg emission rates, as there are a number of large scale industries and coal-fired power plants in India (Burger Chakraborty et al., 2013;Pervez et al., 2010). Additionally, the biomass burning in Southeast Asia should be a large contributor of high TGM levels at ALS (Wang et al., 2015). A small region in eastern Myanmar and northern Laos and Thailand was also identified as a potential source region and pathway for TGM at ALS. The high CWT values in this area may be primarily due to high Hg emission rates because of biomass burning during the non-ISM period.

Indeed, the emission of Hg from biomass burning includes forest fire and agricultural waste burning in Southeast Asia and southwestern China and could also play an important role in TGM distribution and transboundary transport at ALS. Southeast Asia and southwestern China are large tropical rain forest areas. During the ISM period, the air had a very high RH and the highest RF. Because the fire events in Southeast Asia and southwestern China were not frequent and the biomass burning for agriculture was not prevalent, less Hg from biomass burning was released into the atmosphere. As shown in Fig. S3a, fire events in Southeast Asia and southwestern China during the ISM period (mainly from June to September 2011) exhibited a much lower frequency, indicating that the significant impact of TGM transport was primarily from anthropogenic Hg emissions. Nevertheless, during the non-ISM period (mainly from December 2011 to April 2012), high-frequency fire events in Southeast Asia and southwestern China were observed (Fig. S3b). Hg emissions from fire events peaked when the most intense biomass burning occurred in Southeast Asia and Southwest China. This increased TGM level at ALS once air masses from these areas were transported to ALS.

4 Conclusions

This study made at ALS suggests a significant impact of monsoonal climates on the distribution and long-range transport of atmospheric Hg in southwestern China and shows a pronounced monsoonal variation with a high TGM level during the ISM period and a low TGM level during the non-ISM period. This seasonal

variation opposes the previous distribution of atmospheric Hg observed in the background sites of southwestern China. This behavior seems to be dominated by the seasonal variation of monsoons and the influence of the long-range and transboundary transport of Hg from high anthropogenic Hg emissions and biomass burning. The high Hg regional sources from inland China were an important factor in the elevated TGM level. Meanwhile, with the economy developing rapidly, anthropogenic Hg emission in Southeast Asia is also increasing. This will elevate the TGM level in the area, including that of southwestern China. Additionally, Hg emitted from India can travel to southwestern China due to the ISM in the summer and a strong south tributary of westerlies during cold seasons. Biomass burning includes high-frequency fire events in Southeast Asia that could play an important role for high TGM levels during the non-ISM period. Thus, the TGM concentrations during different seasons in addition to the impacts of monsoonal climate may pose an important constraint on the global models of atmospheric Hg.

Acknowledgments. This work is supported by the National "973" Program of China (2013CB430003), the National Science Foundation of China (41430754, 41473025, 41273145，41173024) and the Global Mercury Observation System (GMOS) as part of FP7 (contract no. 265113) funded by the European Commission. We also thank Xin Luo, Ben Yu and Jun Zhou for field sampling assistance.

Reference

AMAP/UNEP: Technical Background Report for the Global Mercury Assessment 2013, in: Arctic Monitoring and Assessment Programme, Oslo, Norway/UNEP Chemicals Branch Geneva, Switzerland, 2013.

Bonasoni, P., Laj, P., Marinoni, A., Sprenger, M., Angelini, F., Arduini, J., Bonafe, U., Calzolari, F., Colombo, T., and Decesari, S.: Atmospheric Brown Clouds in the Himalayas: first two years of continuous observations at the Nepal-Climate Observatory at Pyramid (5079 m), Atmospheric Chemistry and Physics Discussions, 10, 4823-4885, 2010, doi:10.5194/acp-10-7515-2010.

Burger Chakraborty, L., Qureshi, A., Vadenbo, C., and Hellweg, S.: Anthropogenic mercury flows in India and impacts of emission controls, Environmental science & technology, 47, 8105-8113, 2013, doi: 10.1021/es401006k.

Chang, S.-S., Lee, W.-J., Wang, L.-C., Lin, N.-H., and Chang-Chien, G.-P.: Influence of the Southeast Asian biomass burnings on the atmospheric persistent organic pollutants observed at near sources and receptor site, Atmospheric Environment, 78, 184-194, 2013, doi:10.1016/j.atmosenv.2012.07.074.

Cheng, I., Zhang, L., Blanchard, P., Dalziel, J., and Tordon, R.: Concentration-weighted trajectory approach to identifying potential sources of speciated atmospheric mercury at an urban coastal site in Nova Scotia, Canada, Atmos Chem Phys, 13, 6031-6048, 10.5194/acp-13-6031-2013, 2013, doi:10.5194/acp-13-6031-2013.

D'Amore, F., Bencardino, M., Cinnirella, S., Sprovieri, F., and Pirrone, N.: Data quality through a web-based QA/QC system: implementation for atmospheric mercury data from the global mercury observation system, Environ Sci-Proc Imp, 17, 1482-1491, 10.1039/c5em00205b, 2015, doi: 10.1039/C5EM00205B.

Fan, H., Hu, J., and He, D.: Trends in precipitation over the low latitude highlands of Yunnan, China, Journal of

Geographical Sciences, 23, 1107-1122, 2013, doi: 10.1007/s11442-013-1066-y.

Feng, X., Sommar, J., Gårdfeldt, K., and Lindqvist, O.: Improved determination of gaseous divalent mercury in ambient air using KCl coated denuders, Fresenius' journal of analytical chemistry, 366, 423-428, 2000, doi: 10.1007/s002160050086.

Feng, X., and Qiu, G.: Mercury pollution in Guizhou, Southwestern China—an overview, Science of the Total Environment, 400, 227-237, 2008, doi:10.1016/j.scitotenv.2008.05.040.

Friedli, H. R., Arellano, A. F., Cinnirella, S., and Pirrone, N.: Initial Estimates of Mercury Emissions to the Atmosphere from Global Biomass Burning, Environ Sci Technol, 43, 3507-3513, 2009, doi: 10.1021/es802703g.

Fu, X., Feng, X., Zhu, W., Wang, S., and Lu, J.: Total gaseous mercury concentrations in ambient air in the eastern slope of Mt. Gongga, South-Eastern fringe of the Tibetan plateau, China, Atmospheric Environment, 42, 970-979, 2008a, doi:10.1016/j.atmosenv.2007.10.018.

Fu, X., Feng, X., Dong, Z., Yin, R., Wang, J., Yang, Z., and Zhang, H.: Atmospheric gaseous elemental mercury (GEM) concentrations and mercury depositions at a high-altitude mountain peak in south China, Atmospheric Chemistry and Physics, 10, 2425-2437, 2010a, doi:10.5194/acp-10-2425-2010.

Fu, X., Feng, X., Liang, P., Zhang, H., Ji, J., and Liu, P.: Temporal trend and sources of speciated atmospheric mercury at Waliguan GAW station, Northwestern China, Atmospheric Chemistry and Physics, 12, 1951-1964, 2012a, doi:10.5194/acp-12-1951-2012.

Fu, X., Feng, X., Shang, L., Wang, S., and Zhang, H.: Two years of measurements of atmospheric total gaseous mercury (TGM) at a remote site in Mt. Changbai area, Northeastern China, Atmospheric Chemistry and Physics, 12, 4215-4226, 2012b, doi:10.5194/acp-12-4215-2012.

Fu, X. W., Zhang, H., Lin, C. J., Feng, X. B., Zhou, L. X., and Fang, S. X.: Correlation slopes of GEM/CO, GEM/CO2, and GEM/CH4 and estimated mercury emissions in China, South Asia, the Indochinese Peninsula, and Central Asia derived from observations in northwestern and southwestern China, Atmos Chem Phys, 15, 1013-1028, 2015, doi:10.5194/acp-15-1013-2015.

Gustin, M. S., Amos, H. M., Huang, J., Miller, M. B., and Heidecorn, K.: Measuring and modeling mercury in the atmosphere: a critical review, Atmos Chem Phys, 15, 5697-5713, 10.5194/acp-15-5697-2015, 2015, doi:10.5194/acp-15-5697-2015.

Hsu, H.-H.: East asian monsoon, in: Intraseasonal Variability in the atmosphere-ocean climate system, Springer, 63-94, 2005, doi: 10.1007/3-540-27250-X_3.

Hsu, Y.-K., Holsen, T. M., and Hopke, P. K.: Comparison of hybrid receptor models to locate PCB sources in Chicago, Atmospheric Environment, 37, 545-562, 2003, doi:10.1016/S1352-2310(02)00886-5.

Huang, J., Miller, M. B., Weiss-Penzias, P., and Gustin, M. S.: Comparison of gaseous oxidized Hg measured by KCl-coated denuders, and nylon and cation exchange membranes, Environ Sci Technol, 47, 7307-7316, 2013a, doi: 10.1021/es4012349

Huang, J. Y., and Gustin, M. S.: Uncertainties of Gaseous Oxidized Mercury Measurements Using KCl-Coated Denuders, Cation-Exchange Membranes, and Nylon Membranes: Humidity Influences, Environ Sci Technol, 49, 6102-6108, 10.1021/acs.est.5b00098, 2015, doi: 10.1021/acs.est.5b00098.

Huang, K., Fu, J. S., Hsu, N. C., Gao, Y., Dong, X., Tsay, S.-C., and Lam, Y. F.: Impact assessment of biomass burning on air quality in Southeast and East Asia during BASE-ASIA, Atmospheric Environment, 78, 291-302, 2013b, doi:10.1016/j.atmosenv.2012.03.048.

Jiang, G.-B., Shi, J.-B., and Feng, X.-B.: Mercury pollution in China, Environmental science & technology, 40, 3672-3678, 2006, doi: 10.1021/es062707c.

Kang, S. C., Huang, J., Wang, F. Y., Zhang, Q. G., Zhang, Y. L., Li, C. L., Wang, L., Chen, P. F., Sharma, C. M., Li, Q., Sillanpaa, M., Hou, J. Z., Xu, B. Q., and Guo, J. M.: Atmospheric Mercury Depositional Chronology Reconstructed from Lake Sediments and Ice Core in the Himalayas and Tibetan Plateau, Environ Sci Technol, 50, 2859-2869, 10.1021/acs.est.5b04172, 2016, doi: 10.1021/acs.est.5b04172.

Kellerhals, M., Beauchamp, S., Belzer, W., Blanchard, P., Froude, F., Harvey, B., McDonald, K., Pilote, M., Poissant, L., and Puckett, K.: Temporal and spatial variability of total gaseous mercury in Canada: results from the Canadian Atmospheric Mercury Measurement Network (CAMNet), Atmospheric Environment, 37, 1003-1011, 2003, doi:10.1016/S1352-2310(02)00917-2.

Kim, K.-H., Ebinghaus, R., Schroeder, W., Blanchard, P., Kock, H., Steffen, A., Froude, F., Kim, M.-Y., Hong, S., and Kim, J.-H.: Atmospheric mercury concentrations from several observatory sites in the Northern Hemisphere, Journal of Atmospheric Chemistry, 50, 1-24, 2005, doi: 10.1007/s10874-005-9222-0.

Kock, H., Bieber, E., Ebinghaus, R., Spain, T., and Thees, B.: Comparison of long-term trends and seasonal variations of atmospheric mercury concentrations at the two European coastal monitoring stations Mace Head, Ireland, and Zingst, Germany, Atmospheric Environment, 39, 7549-7556, 2005, doi:10.1016/j.atmosenv.2005.02.059.

Landis, M. S., Stevens, R. K., Schaedlich, F., and Prestbo, E. M.: Development and characterization of an annular denuder methodology for the measurement of divalent inorganic reactive gaseous mercury in ambient air, Environmental science & technology, 36, 3000-3009, 2002, doi: 10.1021/es015887t.

Lawrence, M., and Lelieveld, J.: Atmospheric pollutant outflow from southern Asia: a review, Atmospheric Chemistry and Physics, 10, 11017-11096, 2010, doi:10.5194/acp-10-11017-2010.

Lee, G. S., Kim, P. R., Han, Y. J., Holsen, T. M., Seo, Y. S., and Yi, S. M.: Atmospheric speciated mercury concentrations on an island between China and Korea: sources and transport pathways, Atmos Chem Phys, 16, 4119-4133, 2016, doi:10.5194/acp-16-4119-2016.

Lelieveld, J. o., Crutzen, P., Ramanathan, V., Andreae, M., Brenninkmeijer, C., Campos, T., Cass, G., Dickerson, R., Fischer, H., and De Gouw, J.: The Indian Ocean experiment: widespread air pollution from South and Southeast Asia, Science, 291, 1031-1036, 2001, doi: 10.1126/science.1057103.

Li, P., Feng, X., Qiu, G., Shang, L., and Li, Z.: Mercury pollution in Asia: a review of the contaminated sites, Journal of Hazardous Materials, 168, 591-601, 2009, doi:10.1016/j.jhazmat.2009.03.031.

Lin, N.-H., Tsay, S.-C., Maring, H. B., Yen, M.-C., Sheu, G.-R., Wang, S.-H., Chi, K. H., Chuang, M.-T., Ou-Yang, C.-F., and Fu, J. S.: An overview of regional experiments on biomass burning aerosols and related pollutants in Southeast Asia: From BASE-ASIA and the Dongsha Experiment to 7-SEAS, Atmospheric Environment, 78, 1-19, 2013, doi:10.1016/j.atmosenv.2013.04.066.

Lindberg, S., Bullock, R., Ebinghaus, R., Engstrom, D., Feng, X., Fitzgerald, W., Pirrone, N., Prestbo, E., and Seigneur, C.: A synthesis of progress and uncertainties in attributing the sources of mercury in deposition, AMBIO: A Journal of the Human Environment, 36, 19-33, 2007, doi: 10.1579/0044-7447(2007)36[19:ASOPAU]2.0.CO;2.

Liu, W., Fox, J. E., and Xu, Z.: Litterfall and nutrient dynamics in a montane moist evergreen broad-leaved forest in Ailao Mountains, SW China, Plant Ecology, 164, 157-170, 2003a, doi: 10.1023/A:1021201012950.

Liu, W. Y., Fox, J. E. D., and Xu, Z. F.: Nutrient budget of a montane evergreen broad-leaved forest at Ailao Mountain National Nature Reserve, Yunnan, southwest China, Hydrol Process, 17, 1119-1134, 2003b, doi: 10.1002/hyp.1184.

Loewen, M., Kang, S., Armstrong, D., Zhang, Q., Tomy, G., and Wang, F.: Atmospheric transport of mercury to the Tibetan Plateau, Environmental science & technology, 41, 7632-7638, 2007, doi: 10.1021/es0710398.

Loewen, M. D., Sharma, S., Tomy, G., Wang, F., Bullock, P., and Wania, F.: Persistent organic pollutants and mercury in the Himalaya, Aquatic Ecosystem Health & Management, 8, 223-233, 2005, doi:10.1080/14634980500220924.

Mukherjee, A. B., Bhattacharya, P., Sarkar, A., and Zevenhoven, R.: Mercury emissions from industrial sources in India and its effects in the environment, in: Mercury Fate and Transport in the Global Atmosphere, Springer, 81-112, 2009, doi: 10.1007/978-0-387-93958-2_4.

Pacyna, E. G., Pacyna, J., Sundseth, K., Munthe, J., Kindbom, K., Wilson, S., Steenhuisen, F., and Maxson, P.: Global emission of mercury to the atmosphere from anthropogenic sources in 2005 and projections to 2020, Atmospheric Environment, 44, 2487-2499, 2010, doi:10.1016/j.atmosenv.2009.06.009.

Pervez, S., Koshle, A., and Pervez, Y.: Study of spatiotemporal variation of atmospheric mercury and its human exposure around an integrated steel plant, India, Atmospheric Chemistry and Physics, 10, 5535-5549, 2010, doi:10.5194/acp-10-5535-2010.

Pirrone, N., Cinnirella, S., Feng, X., Finkelman, R. B., Friedli, H. R., Leaner, J., Mason, R., Mukherjee, A. B., Stracher, G., and Streets, D. G.: Global mercury emissions to the atmosphere from natural and anthropogenic sources, in: Mercury fate and transport in the global atmosphere, Springer, 1-47, 2009, doi:10.1007/978-0-387-93958-2_1.

Pirrone, N., Cinnirella, S., Feng, X., Finkelman, R., Friedli, H., Leaner, J., Mason, R., Mukherjee, A., Stracher, G., and Streets, D.: Global mercury emissions to the atmosphere from anthropogenic and natural sources, Atmospheric Chemistry and Physics, 10, 5951-5964, 2010, doi:10.5194/acp-10-5951-2010.

Rajgopal, T.: Mercury pollution in India, The Lancet, 362, 1856-1857, 2003, doi: 10.1016/S0140-6736(03)14936-7.

Reid, J. S., Hyer, E. J., Johnson, R. S., Holben, B. N., Yokelson, R. J., Zhang, J., Campbell, J. R., Christopher, S. A., Di Girolamo, L., and Giglio, L.: Observing and understanding the Southeast Asian aerosol system by remote sensing: An initial review and analysis for the Seven Southeast Asian Studies (7SEAS) program, Atmospheric Research, 122, 403-468, 2013, doi:10.1016/j.atmosres.2012.06.005.

Schroeder, W. H., and Munthe, J.: Atmospheric mercury—an overview, Atmospheric Environment, 32, 809-822, 1998, doi:10.1016/S1352-2310(97)00293-8.

Sheu, G.-R., Lin, N.-H., Wang, J.-L., Lee, C.-T., Ou Yang, C.-F., and Wang, S.-H.: Temporal distribution and potential sources of atmospheric mercury measured at a high-elevation background station in Taiwan, Atmospheric

577 Environment, 44, 2393-2400, 2010a, doi:10.1016/j.atmosenv.2010.04.009.
578 Sheu, G.-R., Lin, N.-H., Lee, C.-T., Wang, J.-L., Chuang, M.-T., Wang, S.-H., Chi, K. H., and Ou-Yang, C.-F.:
579 Distribution of atmospheric mercury in northern Southeast Asia and South China Sea during Dongsha Experiment,
580 Atmospheric Environment, 78, 174-183, 2013, doi:10.1016/j.atmosenv.2012.07.002.
581 Sigler, J. M., Lee, X., and Munger, W.: Emission and long-range transport of gaseous mercury from a large-scale
582 Canadian boreal forest fire, Environ Sci Technol, 37, 4343-4347, 2003, doi: 10.1021/es026401r.
583 Slemr, F., Angot, H., Dommergue, A., Magand, O., Barret, M., Weigelt, A., Ebinghaus, R., Brunke, E. G., Pfaffhuber,
584 K. A., Edwards, G., Howard, D., Powell, J., Keywood, M., and Wang, F.: Comparison of mercury concentrations
585 measured at several sites in the Southern Hemisphere, Atmos Chem Phys, 15, 3125-3133, 2015,
586 doi:10.5194/acp-15-3125-2015.
587 Sprovieri, F., Pirrone, N., Ebinghaus, R., Kock, H., and Dommergue, A.: A review of worldwide atmospheric
588 mercury measurements, Atmospheric Chemistry and Physics, 10, 8245-8265, 2010, doi:10.5194/acp-10-8245-2010.
589 Sprovieri, F., Gratz, L., and Pirrone, N.: Development of a Ground-Based Atmospheric Monitoring Network for the
590 Global Mercury Observation System (GMOS), E3S Web of Conferences, 2013, 17007, doi:
591 http://dx.doi.org/10.1051/e3sconf/20130117007.
592 Swartzendruber, P. C., Jaffe, D. A., and Finley, B.: Improved fluorescence peak integration in the Tekran 2537 for
593 applications with sub-optimal sample loadings, Atmos Environ, 43, 3648-3651, 2009,
594 doi:10.1016/j.atmosenv.2009.02.063.
595 Tseng, C., Liu, C.-S., and Lamborg, C.: Seasonal changes in gaseous elemental mercury in relation to monsoon
596 cycling over the northern South China Sea, Atmospheric Chemistry and Physics, 12, 7341-7350, 2012,
597 doi:10.5194/acp-12-7341-2012.
598 Venter, A. D., Beukes, J. P., van Zyl, P. G., Brunke, E. G., Labuschagne, C., Slemr, F., Ebinghaus, R., and Kock, H.:
599 Statistical exploration of gaseous elemental mercury (GEM) measured at Cape Point from 2007 to 2011, Atmos
600 Chem Phys, 15, 10271-10280, 2015, doi:10.5194/acp-15-10271-2015.
601 Wang, C., Kim, D., Ekman, A. M., Barth, M. C., and Rasch, P. J.: Impact of anthropogenic aerosols on Indian
602 summer monsoon, Geophysical Research Letters, 36, 2009, doi: 10.1029/2009GL040114.
603 Wang, D., He, L., Wei, S., and Feng, X.: Estimation of mercury emission from different sources to atmosphere in
604 Chongqing, China, Science of the total environment, 366, 722-728, 2006, doi:10.1016/j.scitotenv.2005.09.054.
605 Wang, X., Zhang, H., Lin, C. J., Fu, X. W., Zhang, Y. P., and Feng, X. B.: Transboundary transport and deposition of
606 Hg emission from springtime biomass burning in the Indo-China Peninsula, J Geophys Res-Atmos, 120, 9758-9771,
607 2015, doi: 10.1002/2015JD023525.
608 Wooster, M. J., Roberts, G., Perry, G. L. W., and Kaufman, Y. J.: Retrieval of biomass combustion rates and totals
609 from fire radiative power observations: FRP derivation and calibration relationships between biomass consumption
610 and fire radiative energy release, J Geophys Res-Atmos, 110, 2005, doi: 10.1029/2005JD006318.
611 Wu, Y., Wang, S., Streets, D. G., Hao, J., Chan, M., and Jiang, J.: Trends in anthropogenic mercury emissions in
612 China from 1995 to 2003, Environmental Science & Technology, 40, 5312-5318, 2006, doi: 10.1021/es060406x.
613 Xiao, Z., Sommar, J., Wei, S., and Lindqvist, O.: Sampling and determination of gas phase divalent mercury in the

air using a KCl coated denuder, Fresenius' journal of analytical chemistry, 358, 386-391, 1997, doi: 10.1007/s002160050434.

Xu, B., Cao, J., Hansen, J., Yao, T., Joswia, D. R., Wang, N., Wu, G., Wang, M., Zhao, H., and Yang, W.: Black soot and the survival of Tibetan glaciers, Proceedings of the National Academy of Sciences, 106, 22114-22118, 2009, doi: 10.1073/pnas.0910444106.

Yao, T., Thompson, L., Yang, W., Yu, W., Gao, Y., Guo, X., Yang, X., Duan, K., Zhao, H., and Xu, B.: Different glacier status with atmospheric circulations in Tibetan Plateau and surroundings, Nature Climate Change, 2, 663-667, 2012, doi:10.1038/nclimate1580.

You, G., Zhang, Y., Liu, Y., Schaefer, D., Gong, H., Gao, J., Lu, Z., Song, Q., Zhao, J., and Wu, C.: Investigation of temperature and aridity at different elevations of Mt. Ailao, SW China, International journal of biometeorology, 1-6, 2012, doi: 10.1007/s00484-012-0570-6.

Yu, B., Wang, X., Lin, C. J., Fu, X. W., Zhang, H., Shang, L. H., and Feng, X. B.: Characteristics and potential sources of atmospheric mercury at a subtropical near-coastal site in East China, J Geophys Res-Atmos, 120, 8563-8574, 10.1002/2015JD023425, 2015, doi: 10.1002/2015JD023425.

Yuhong, Z. K. M. Y. L., and Yourong, L.: Agriculture significance of the foehn effect in the SW monsoon:A case study in the Ailao mountain, Journal of Mountain Research, 2, 002, 1993.

Zhang, G., Li, J., Li, X.-D., Xu, Y., Guo, L.-L., Tang, J.-H., Lee, C. S., Liu, X., and Chen, Y.-J.: Impact of anthropogenic emissions and open biomass burning on regional carbonaceous aerosols in South China, Environmental Pollution, 158, 3392-3400, 2010, doi:10.1016/j.envpol.2010.07.036.

Zhang, H., Yin, R.-s., Feng, X.-b., Sommar, J., Anderson, C. W., Sapkota, A., Fu, X.-w., and Larssen, T.: Atmospheric mercury inputs in montane soils increase with elevation: evidence from mercury isotope signatures, Scientific reports, 3, 2013, doi: 10.1038/srep03322.

Zhang, H., Fu, X. W., Lin, C. J., Wang, X., and Feng, X. B.: Observation and analysis of speciated atmospheric mercury in Shangri-La, Tibetan Plateau, China, Atmos Chem Phys, 15, 653-665, 2015, doi:10.5194/acp-15-653-2015.

Zhang, Q. G., Huang, J., Wang, F. Y., Mark, L. W., Xu, J. Z., Armstrong, D., Li, C. L., Zhang, Y. L., and Kang, S. C.: Mercury Distribution and Deposition in Glacier Snow over Western China, Environ Sci Technol, 46, 5404-5413, 2012, doi: 10.1021/es300166x.

Zhao, D., Yao, P., Yang, R.W., and Cao, J.: The spatial and temporal distribution features of onset period of mean rainy season over Asian monsoon region, Journal of Yunnan University (Natural Sciences Edition), 4, 012, 2006.

651 **Figure Captions**

652

653 **Table 1:** The statistics for mercury species and meteorological variables based on daily averages from May
654 2010 through May 2011 at the ALS site.

655 **Fig. 1:** Map showing the location of ALS, anthropogenic mercury emissions (g km^{-2} y^{-1}) and major cities in
656 Asia (AMAP/UNEP, 2013).

657 **Fig. 2:** Total gaseous mercury (TGM) concentration in the ambient air at ALS. Source 1 represents the peaks
658 of high TGM concentrations at ALS during the ISM period, which were caused by anthropogenic Hg
659 emissions from inland China due to the strengthening of EASM. Source 2 represents the peaks of high TGM
660 concentrations at ALS during the non-ISM period, which were caused by the biomass burning from Southeast
661 Asia and anthropogenic Hg emissions from South Asia.

662 **Fig. 3:** Distribution frequency of TGM above and under the average (2.09 ng m^{-3}) based on wind direction
663 during the ISM and the non-ISM period. The high and low Hg levels of the SW frequency was higher than
664 both the high and low Hg levels of the NE and SE frequencies.

665 **Fig. 4:** Monthly TGM anomalies at ALS. The Hg concentration during the ISM period (May to September)
666 was higher than that of the non-ISM period (October to April). The highest monthly concentration (2.46 ng m^{-3})
667 was observed in May, and the lowest monthly mean concentration (1.45 ng m^{-3}) was observed in November.
668 The air temperature was higher, and the wind speed was lower during the ISM period than that of the non-ISM
669 period.

670 **Fig. 5:** TGM, GOM and PBM variation during the ISM and non-ISM period based on the four sampling
671 campaigns. TGM, GOM and PBM concentrations showed a monsoonal variation with higher level during the
672 ISM period than in the non-ISM period.

673 **Fig. 6:** Pollution roses of Hg species. Most of the TGM, GOM and PBM were from SW, and some higher
674 TGM, GOM and PBM events were from NE during the ISM period. Almost all TGM, GOM and PBM were
675 from SW during the non-ISM period.

676 **Fig. 7:** Air mass backward trajectory analysis for long range transport to ALS. Most of these backward
677 trajectories consisted of air masses that originated from South and Southeast Asia and were accompanied by
678 lower Hg levels. Air masses originating from inland China were less frequent and accompanied by higher Hg
679 levels.

680 **Fig. 8:** The distribution of the Indian monsoon index (IMI), TGM and rainfall at ALS. IMI displays that the
681 ISM period was from May to September. RF events mainly appeared during the ISM period. Some high Hg
682 events were accompanied by NE and east wind events during the ISM period. High TGM events were
683 accompanied by the appearance of SW during the non-ISM period.

684 **Fig. 9:** Backward trajectories of air masses and the variation of TGM concentrations because of the
685 strengthening of and incursion of air flow from EASM on June 23-28, 2011 (a), and July 10-18, 2011 (b),
686 during the ISM period (May to September). The TGM level (C) were 3.27 ng m^{-3}(a) and 3.65 ng m^{-3}(b) with

687 the air masses from important industrial regions of inland China. The TGM level were down to 2.49 ng m^{-3}(a)
688 and 3.02 ng m^{-3}(b) while the air flow shifted to southwest and swept Southeast Asia.
689 **Fig. 10:** Backward trajectories of air masses and the variation of TGM concentrations because of the
690 strengthening and incursion of air flow from EASM and the cold Siberian current from September 28 to
691 October 9, 2011, during the non-ISM period (October to April). The TGM level (C) were 2.25 ng m^{-3}, 3.18 ng
692 m^{-3} and 2.53 ng m^{-3} with the air masses from inland China. The TGM level was down to 1.89 ng m^{-3} with the
693 air masses from South China Sea, northern Vietnam and Laos.
694 **Fig. 11:** Backward trajectories of air masses and the sites of fire events from December 23-31, 2011, during the
695 non-ISM period (October to April). The TGM level (C) was 3.13 ng m^{-3} with air masses from important
696 Southeast Asia industrial regions. The TGM level dropped to 2.78 ng m^{-3} with air masses from the Bay of
697 Bengal.
698 **Fig. 12:** Correlation of TGM and CO in December 23-31, 2011, during the non-ISM period.
699 **Fig. 13:** Backward trajectories of air masses and the sites of fire events in March 23-29, 2012, during the
700 non-ISM period (October to April). The TGM level (C) were 4.53 ng m^{-3} with the air masses from inland
701 China. The TGM level was 3.11 ng m^{-3} with the air masses from Myanmar and high-frequency fire events.
702 **Fig. 14:** Correlation of TGM and CO (R^2=0.53), correlations between TFRP (total fire radiative power) and
703 CO (R^2=0.98) and TGM (R^2=0.45) in March 23-29, 2012, during the non-ISM period (October to April).
704 **Fig. 15:** Potential source regions and pathways of atmospheric TGM at ALS as identified by the CWT during
705 the ISM period (a, May to September) and the non-ISM period (b, October to April).
706

Table 1: The statistics for mercury species and meteorological variables based on daily averages from May 2010 through May 2011 at the ALS site.

		Spring	Summer	Autumn	Winter	ISM period	Non-ISM period	Total
TGM ($ng\ m^{-3}$)	Mean	2.18	2.20	1.92	2.04	2.22	1.99	2.09
	±SD	0.67	0.60	0.64	0.58	0.58	0.66	0.63
	Range	1.01-5.70	1.15-3.79	1.11-3.59	0.99-4.45	1.01-3.79	0.99-5.70	0.99-5.70
GOM ($pg\ m^{-3}$)	Mean	2.31	2.04	3.42	1.83	2.45	2.06	2.22
	±St.Dev	1.79	1.39	2.99	2.85	2.08	2.40	2.28
	Range	0.13-10.20	0.27-6.68	0.11-13.29	0.12-17.25	0.11-13.29	0.12-17.25	0.11-17.25
PBM ($pg\ m^{-3}$)	Mean	22.39	32.19	46.28	31.97	36.38	27.36	31.27
	±St.Dev	19.05	30.56	28.80	30.63	30.62	26.09	28.44
	Range	0.87-135.79	5.84-165.01	16.16-120.99	3.84-139.65	5.84-165.01	0.87-139.65	0.87-165.01
AT (˚C)	Mean	13.36	15.53	11.42	6.96	15.45	8.93	11.95
	±St.Dev	3.03	1.19	3.39	1.88	1.29	2.93	3.99
	Range	4.88-18.38	11.66-17.74	4.78-16.18	1.65-10.83	11.32-18.38	1.65-15.16	1.65-18.38
RH (%)	Mean	72.26	90.77	91.11	73.58	87.43	75.77	81.17
	±St.Dev	15.06	5.56	4.94	18.17	9.58	17.48	15.49
	Range	38.42-97.63	71.17-99.25	79.96-100.00	33.17-100.00	52.25-99.25	33.17-100.00	33.17-100.00
WS (m/s)	Mean	3.60	2.59	2.71	4.29	2.59	3.80	3.29
	±St.Dev	0.42	0.47	0.38	0.07	0.45	0.55	0.79
	Range	2.99-3.95	2.05-3.19	2.17-2.97	4.20-4.37	2.05-3.19	2.97-4.37	2.05-4.37
RF (mm)	Total	334.3	845.4	612.4	44.2	1493	343.3	1836.3
CO (ppbv)	Mean	286		213.9	211.6		254.9	254.9
	±St.Dev	116.1		79.5	90.4		111.1	111.1
WD (%)	NE	3.25	15.22	14.03	0	11.35	5.46	7.79
	SE	9.76	14.13	20.65	4.0	16.22	10.33	13.07
	SW	86.99	66.30	64.13	95.60	71.89	84.98	78.89
	NW	0	0	0	0	0	0	0

712 **Fig. 1:** Map showing the location of ALS, anthropogenic mercury emissions (g km^{-2} y^{-1}) and major cities in
713 Asia (AMAP/UNEP, 2013).

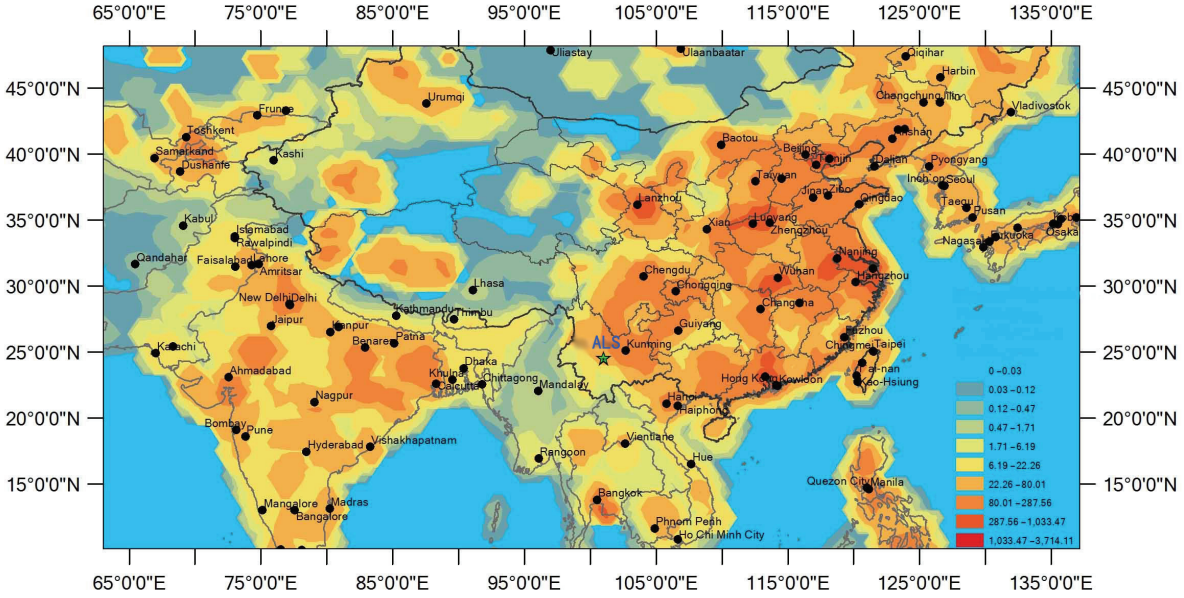

714

715

716 **Fig. 2:** Total gaseous mercury (TGM) concentration in the ambient air at ALS. Source 1 represents the peaks
717 of high TGM concentrations at ALS during the ISM period (May to September), which were caused by
718 anthropogenic Hg emissions from inland China due to the strengthening of EASM. Source 2 represents the
719 peaks of high TGM concentrations at ALS during the non-ISM period (October to April), which were caused
720 by the biomass burning from Southeast Asia and anthropogenic Hg emissions from South Asia.
721

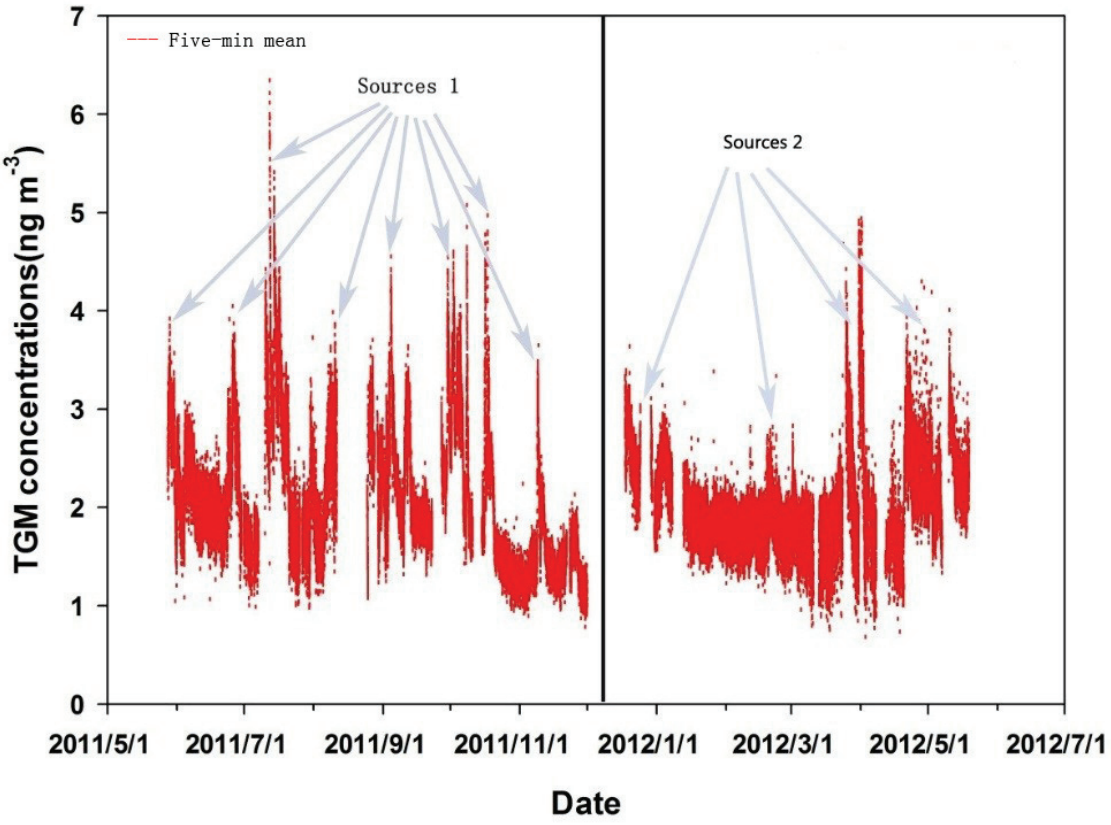

722
723

Fig. 3: Distribution frequency of TGM above and under the average (2.09 ng m^{-3}) based on wind direction during the ISM (May to September) and the non-ISM period (October to April). The high and low TGM levels of the SW frequency was higher than both the high and low TGM levels of the NE and SE frequencies.

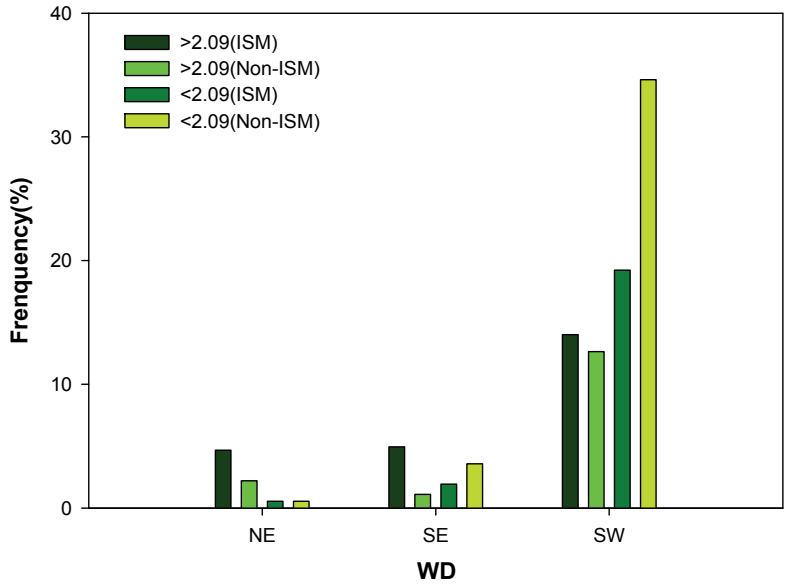

738 **Fig. 4:** Monthly TGM anomalies at ALS. The TGM concentration during the ISM period (May to September)
739 was higher than that of the non-ISM period (October to April). The highest monthly concentration (2.46 ng m^{-3})
740 was observed in May, and the lowest monthly mean concentration (1.45 ng m^{-3}) was observed in November.
741 The air temperature was higher, and the wind speed was lower during the ISM period than that of the non-ISM
742 period.
743

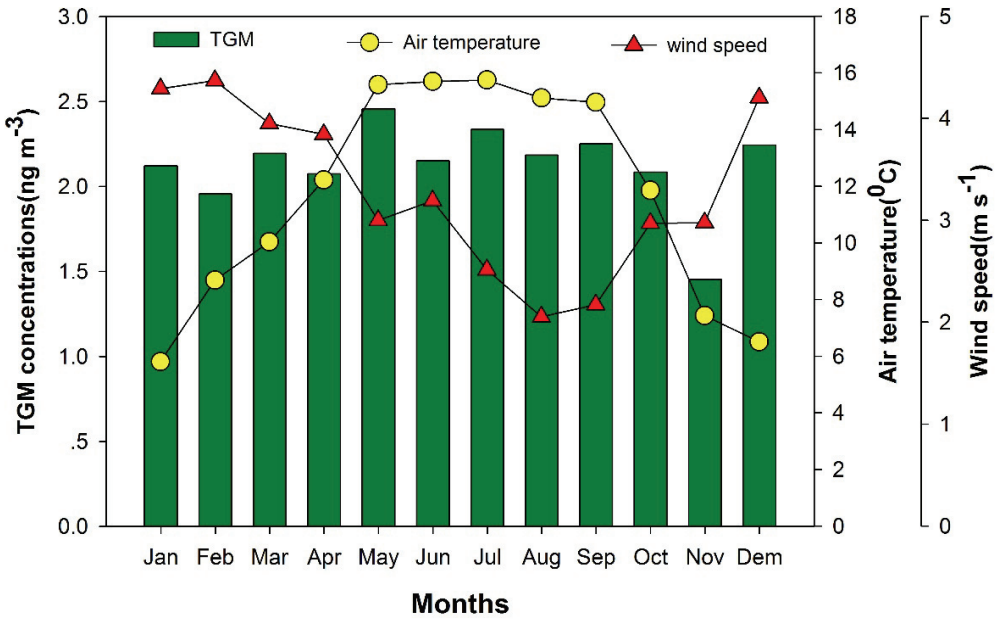

744
745

Fig. 5: TGM, GOM and PBM variation during the ISM (May to September) and non-ISM period (October to April) based on the four sampling campaigns. TGM, GOM and PBM concentrations showed a monsoonal variation with higher level during the ISM period than in the non-ISM period.

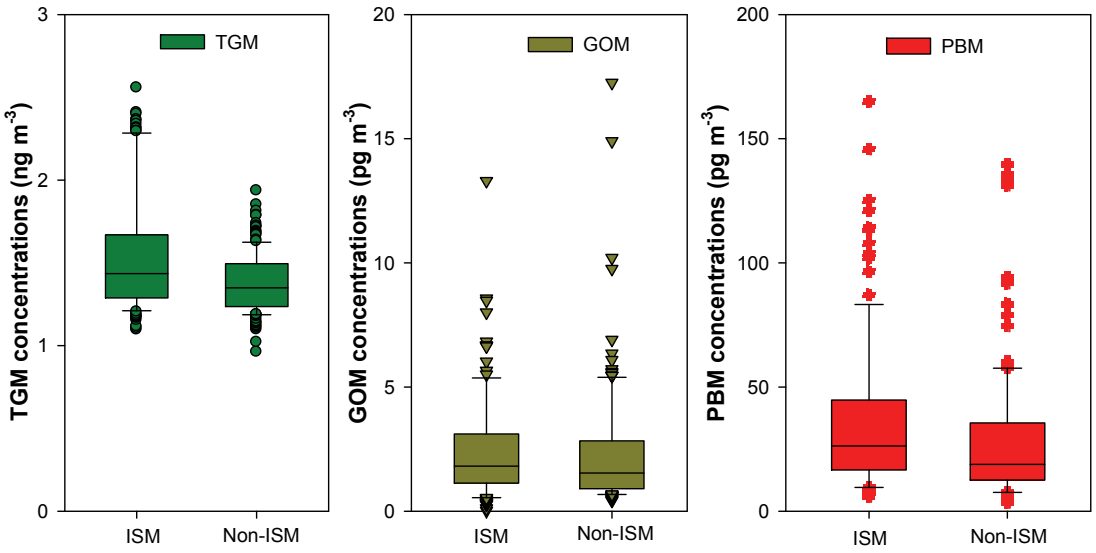

750 **Fig. 6:** Pollution roses of Hg species. Most of the TGM, GOM and PBM were from SW, and some higher
751 TGM, GOM and PBM events were from NE during the ISM period (May to September). Almost all TGM,
752 GOM and PBM were from SW during the non-ISM period (October to April).
753

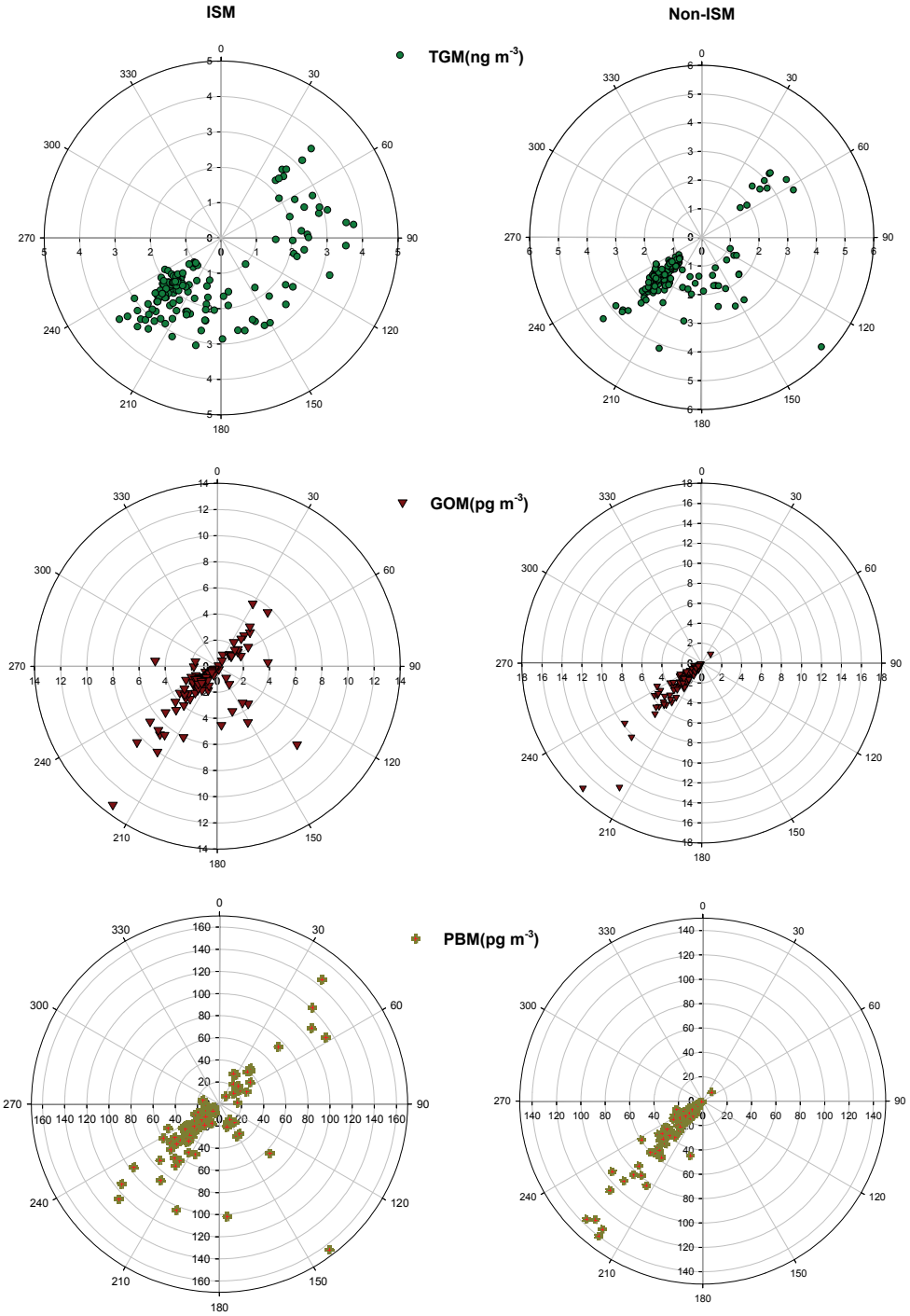

754

Fig. 7: Air mass backward trajectory analysis for long range transport to ALS. Most of these backward trajectories consisted of air masses that originated from South and Southeast Asia and were accompanied by lower TGM levels. Air masses originating from inland China were less frequent and accompanied by higher TGM levels.

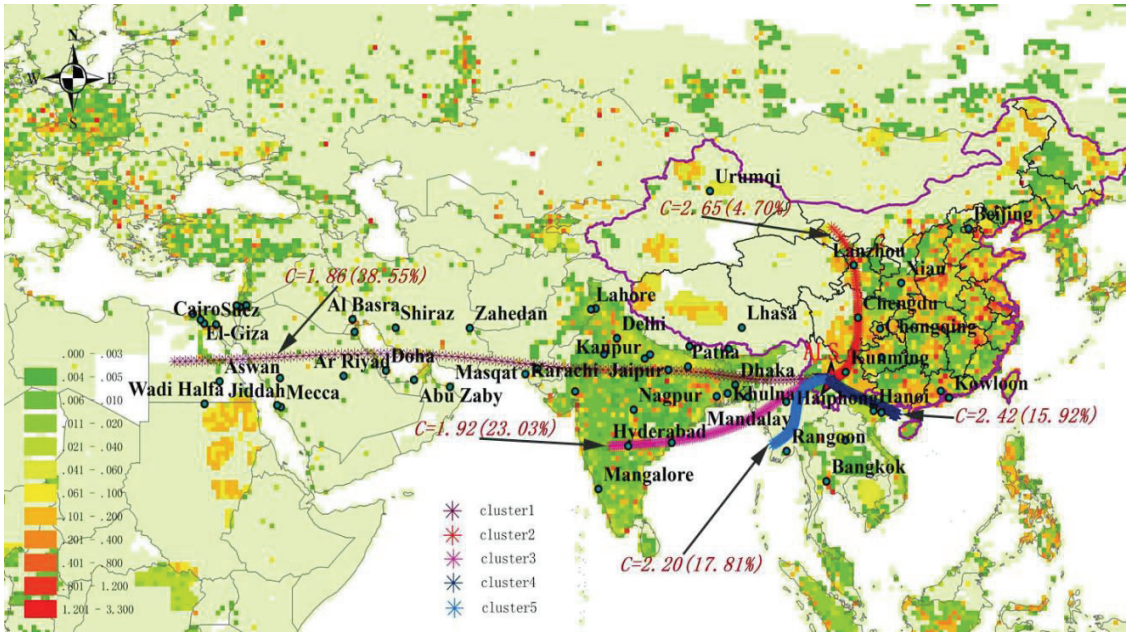

Fig. 8: The distribution of the Indian monsoon index (IMI), TGM and rainfall at ALS. IMI displays that the ISM period was from May to September. RF events mainly appeared during the ISM period. Some high TGM events were accompanied by NE and east wind events during the ISM period. High TGM events were accompanied by the appearance of SW during the non-ISM period (October to April).

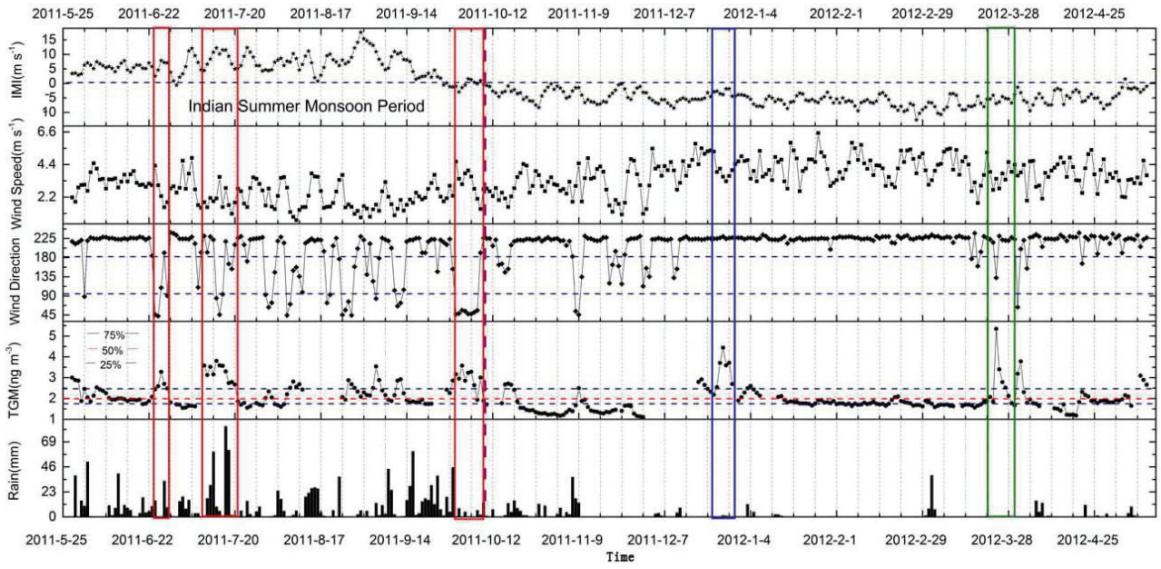

Fig. 9: Backward trajectories of air masses and the variation of TGM concentrations because of the strengthening of and incursion of air flow from EASM on June 23-28, 2011 (a), and July 10-18, 2011 (b), during the ISM period (May to September). The TGM level (C) were 3.27 ng m^{-3}(a) and 3.65 ng m^{-3}(b) with the air masses from important industrial regions of inland China. The TGM level were down to 2.49 ng m^{-3}(a) and 3.02 ng m^{-3}(b) while the air flow shifted to southwest and swept Southeast Asia.

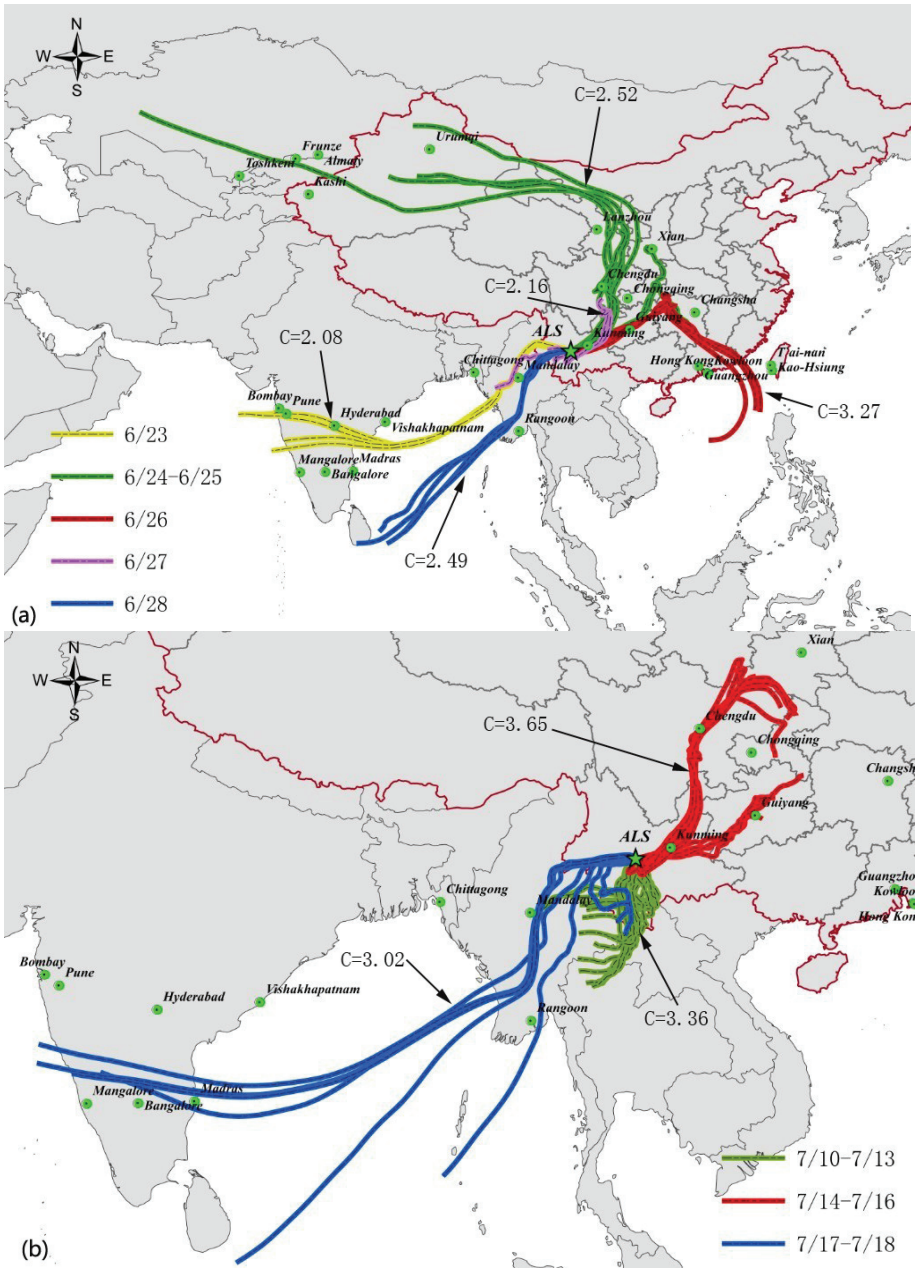

Fig. 10: Backward trajectories of air masses and the variation of TGM concentrations because of the strengthening and incursion of air flow from EASM and the cold Siberian current from September 28 to October 9, 2011, during the non-ISM period (October to April). The TGM level (C) were 2.25 ng m^{-3}, 3.18 ng m^{-3} and 2.53 ng m^{-3} with the air masses from inland China. The TGM level was down to 1.89 ng m^{-3} with the air masses from South China Sea, northern Vietnam and Laos.

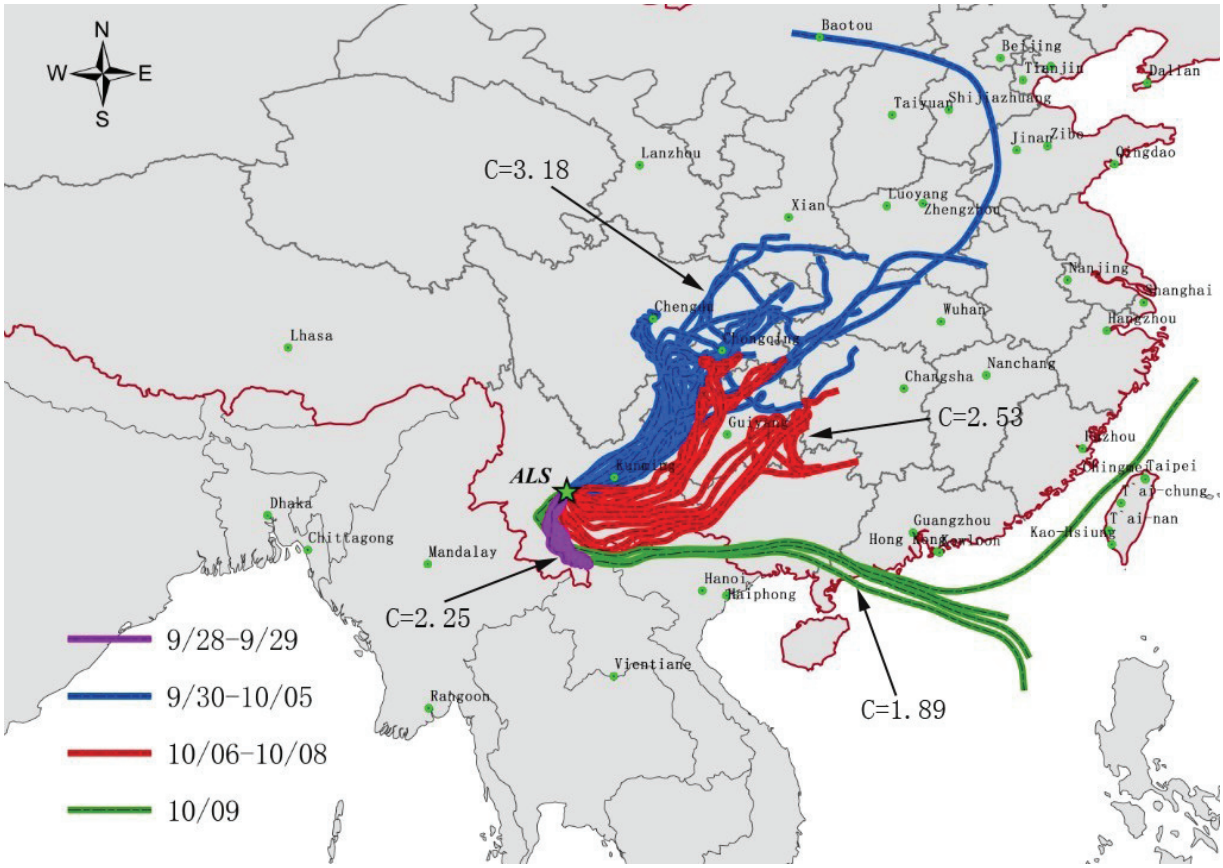

Fig. 11: Backward trajectories of air masses and the sites of fire events from December 23-31, 2011 (https://firms.modaps.eosdis.nasa.gov/firemap/), during the non-ISM period (October to April). The TGM level (C) was 3.13 ng m^{-3} with air masses from important Southeast Asia industrial regions. The TGM level dropped to 2.78 ng m^{-3} with air masses from the Bay of Bengal.

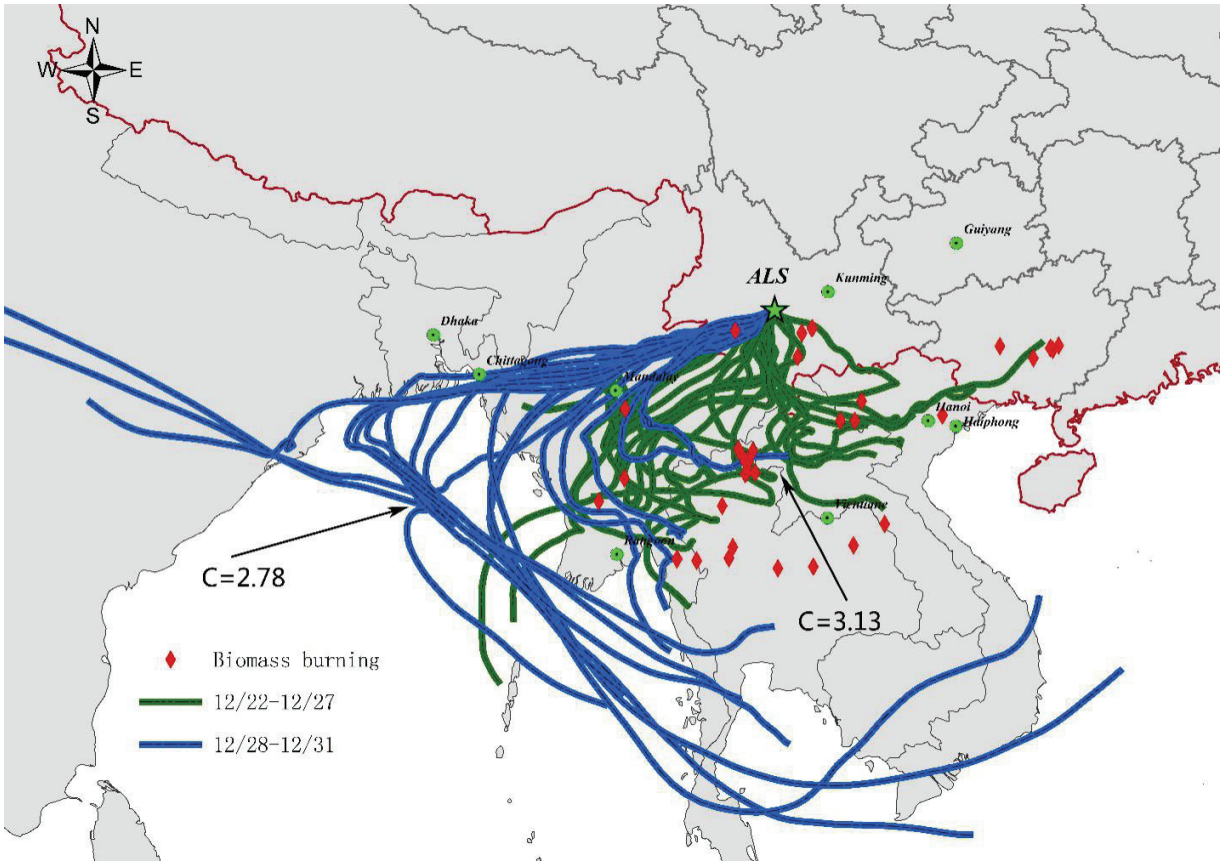

794 **Fig. 12:** Correlation of TGM and CO in December 23-31, 2011, during the non-ISM period (October to April).
795

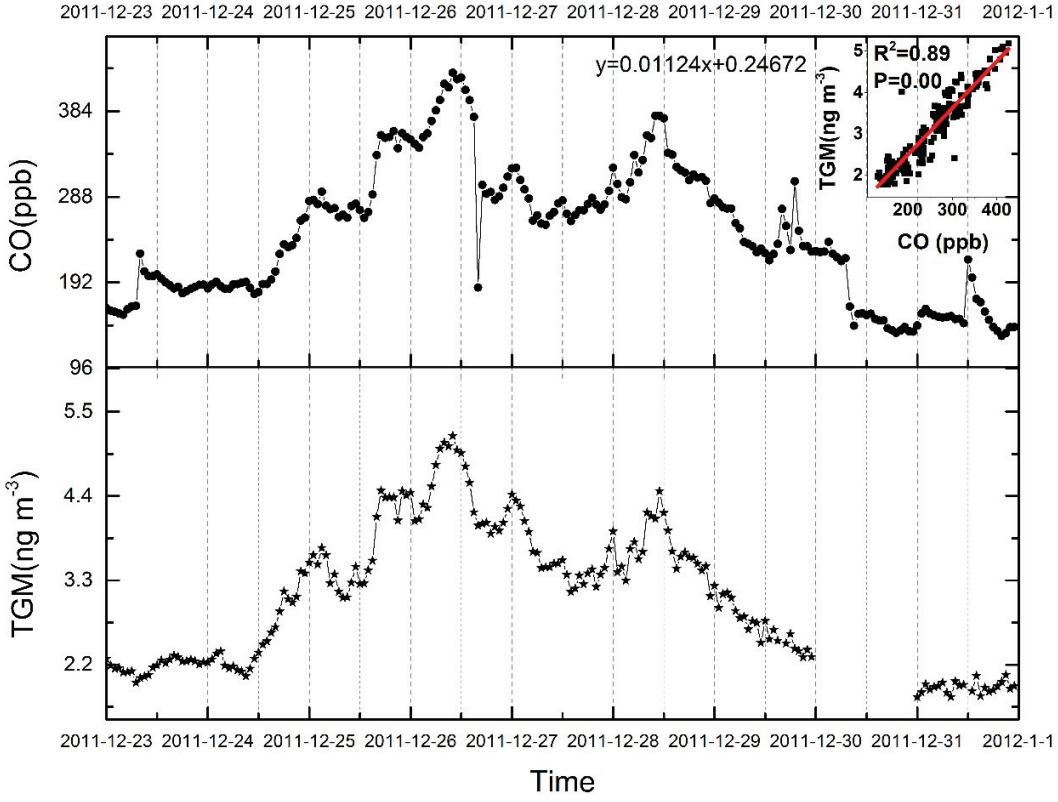

796
797

Fig. 13: Backward trajectories of air masses and the sites of fire events in March 23-29, 2012 (https://firms.modaps.eosdis.nasa.gov/firemap/), during the non-ISM period (October to April). The TGM level (C) were 4.53 ng m^{-3} with the air masses from inland China. The TGM level was 3.11 ng m^{-3} with the air masses from Myanmar and high-frequency fire events.

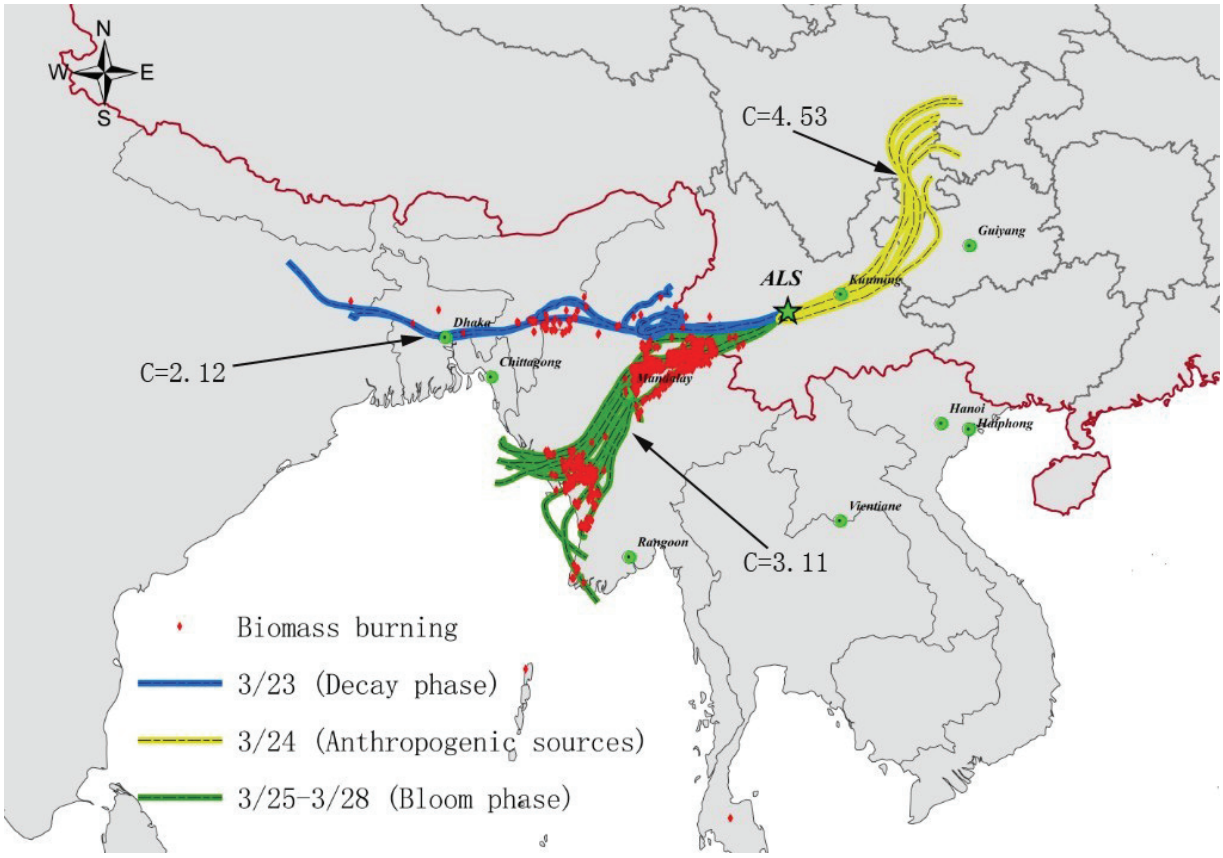

805 **Fig. 14:** Correlation of TGM and CO (R^2=0.53), correlations between TFRP (total fire radiative power) and
806 CO (R^2=0.98) and TGM (R^2=0.45) in March 23-29, 2012, during the non-ISM period (October to April).
807

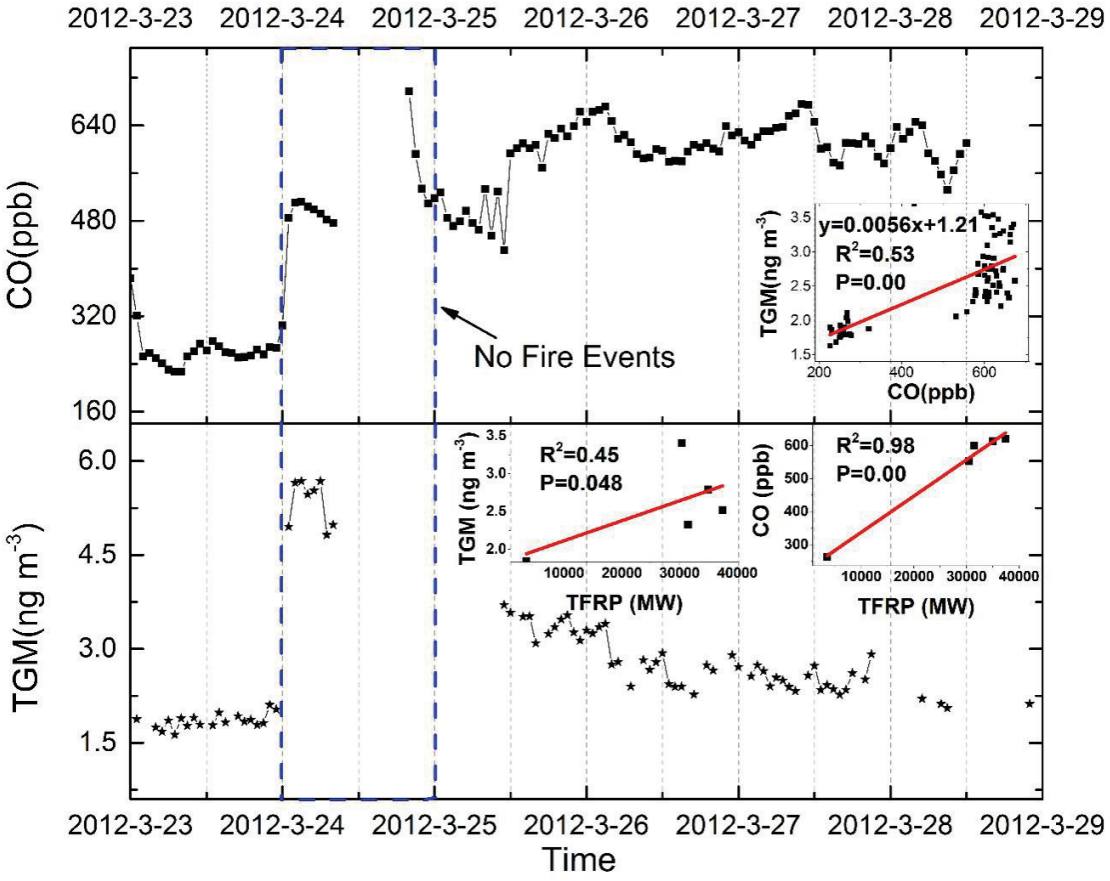

808
809

Fig. 15: Potential source regions of atmospheric TGM at ALS as identified by the CWT during the ISM period (a, May to September) and the non-ISM period (b, October to April).